Higher Order Frequency-Domain Computational Electromagnetics

Branislav M. Notaroš, *Senior Member, IEEE*

(Invited Review Paper)

***Abstract*—A review of the higher order computational electromagnetics (CEM) for antenna, wireless, and microwave engineering applications is presented. Higher order CEM techniques use current/field basis functions of higher orders defined on large (e.g., on the order of a wavelength in each dimension) curvilinear geometrical elements, which greatly reduces the number of unknowns for a given problem. The paper reviews all major surface/volume integral- and differential-equation electromagnetic formulations within a higher order computational framework, focusing on frequency-domain solutions. With a systematic and unified review of generalized curved parametric quadrilateral, triangular, hexahedral, and tetrahedral elements and various types of higher order hierarchical and interpolatory vector basis functions, in both divergence- and curl-conforming arrangements, a large number of actual higher order techniques, representing various combinations of formulations, elements, bases, and solution procedures, are identified and discussed. The examples demonstrate the accuracy, efficiency, and versatility of higher order techniques, and their advantages over low-order discretizations, the most important one being a much faster (higher order) convergence of the solution. It is demonstrated that both components of the higher order modeling, namely, higher order geometrical modeling and higher order current/field modeling, are essential for accurate and efficient CEM analysis of general antenna, scattering, and microwave structures.**

***Index Terms*—Antennas, curved parametric elements, differential-equation techniques, electromagnetic analysis, fast methods, finite element method (FEM), higher order modeling, hybrid methods, integral-equation techniques, method of moments (MoM), numerical techniques, polynomial basis functions, scattering.**

I. Introduction

THE importance of computational electromagnetics (CEM) to antenna, microwave, and wireless technologies can hardly be overstated. CEM simulations are nowadays effectively used at frequencies spanning dc to optics, for system sizes ranging from subatomic to intergalactic, and for such a broad spectrum of application areas as design of antennas and RF/microwave devices, components, and circuits, electromagnetic scattering, wireless communication systems, remote sensing, electromagnetic compatibility, signal integrity, high-speed electronics, new materials, nanoelectromagnetics, and bioelectromagnetics. CEM techniques can broadly be classified into those based on integral-equation (IE) formulations [1]–[5], those based on differential-equation (DE) formulations [5]–[13], and hybrid techniques combining the IE and DE approaches [5]–[9]. On the other side, as the general numerical discretization procedures for transforming the integral and differential equations into a matrix equation, and ultimately into a solution to the problem, the CEM uses the method of moments (MoM) [1] to discretize IEs and both finite element method (FEM) [6] and finite-difference time-domain (FDTD) method [11] to discretize DEs, in addition to other approaches, including (but not limited to) the transmission-line modeling (TLM) method [13]–[15], multiresolution time-domain (MRTD) method [16]–[18], and finite integration technique (FIT) [19], [20]. Overall, MoM, FEM, FDTD, TLM, MRTD, and FIT algorithms, with different IE and DE formulations, are extremely powerful and versatile general CEM methodologies for electromagnetic simulations.

However, in terms of the particulars of the numerical discretizations, traditional CEM tools are low-order (also referred to as small-domain or subdomain) techniques – the structure is modeled by surface and/or volume geometrical elements that are electrically very small and the currents and/or fields within the elements are approximated by low-order basis functions. More precisely, the elements are on the order of $\lambda/10$ in each dimension, λ being the wavelength in the medium, and the basis functions are complete to the lowest order (zeroth order). This results in a very large number of unknowns (unknown current/field distribution coefficients) needed to obtain results of satisfactory accuracy, with all the associated problems and enormous requirements in computational resources. Equivalently, low-order bases exhibit a low (low-order) convergence rate of the solution – the accuracy of the solution is improved slowly with increasing the number of unknowns. In addition, commonly used geometrical elements are in the form of flat triangular and quadrilateral patches for surface modeling, and those for volumetric modeling include bricks, tetrahedra, and triangular prisms, all with planar sides, and thus such elements

Manuscript received August 3, 2007; revised November 29, 2007. Published August 6, 2008 (projected). This work was supported by the National Science Foundation under Grant ECS-0115756, Grant ECCS-0647380, and Grant ECCS-0650719.

The author is with the Department of Electrical and Computer Engineering, Colorado State University, Fort Collins, CO 80523-1373 USA (e-mail: notaros@colostate.edu).

Color versions of one or more of the figures in this paper are available online at http://ieeexplore.ieee.org.

Digital Object Identifier 10.1109/TAP.2008.926784

do not provide enough flexibility and efficiency in modeling of structures with pronounced curvature.

An alternative which can greatly reduce the number of unknowns for a given problem and enhance the accuracy and efficiency of the CEM analysis in different IE, DE, and hybrid formulations is the higher order (also known as the large-domain or entire-domain) computational approach. This approach utilizes higher order basis functions defined in large geometrical elements (e.g., on the order of λ in each dimension), which enables faster (higher order) convergence of the solution. For CEM modeling of general structures that may possess arbitrary curvature, it is essential to have both higher order geometrical flexibility and higher order current/field-approximation flexibility in the same method. In other words, if higher order basis functions for currents/fields are used on flat surface elements or volume elements with flat sides, many small elements may be required for the geometrical precision of the model, and then higher order basis functions actually reduce to low-order functions (on small elements). On the other hand, geometrical flexibility of curved elements can be fully exploited only if they can be made electrically large, which implies the use of higher order current/field expansions within the elements as well. Finally, in order to make the modeling of realistic structures optimal, it is often convenient to have elements of different orders and sizes combined together in the same model.

Although the higher order CEM has a history of almost 40 years, with one of the first higher order MoM techniques being that for wire-dipole antenna analysis in [21], one of the first higher order FEM solutions that to a general waveguide problem in [22], and one of the first modeling techniques using curved elements that for IE analysis of arbitrary metallic antennas and scatterers in [23], only relatively recently the CEM community has started to very extensively investigate and employ higher order surface and volume elements and higher order basis functions. A number of higher order techniques have been proposed and described in the frame of MoM, including surface integral equation (SIE) formulations [2]–[4], [24]–[67], volume integral equation (VIE) formulations [68]–[77], and volume-surface integral equation (VSIE) formulations [9], [41], [78], [79], FEM [6], [7], [9], [24], [25], [80]–[119], FDTD method [120]–[130], MRTD method [17], [18], and FIT [131]. They have already proved to be an efficient and reliable resource for solving large and complex electromagnetic problems in a variety of emerging areas of science and engineering. Higher order electromagnetic modeling is definitely becoming the mainstream of activity in CEM, with many important research challenges yet to be addressed and solved in a quest to achieve more speed, accuracy, and versatility of CEM simulations, with a common goal to create an ultimate, "ideal" analysis and design tool for each given class of real-world applications, and each given engineering problem.

This paper reviews the higher order CEM for antenna, wireless, and microwave engineering applications. It discusses the state of the art in this important area, and aims at providing as complete and unified as possible representation of fundamental aspects and recent advances across a spectrum of higher order CEM formulations, geometrical elements, basis functions, and solution techniques. However, given the wealth and diversity of available and emerging higher order CEM methods and codes, this review is by no means meant as an exhaustive survey, but rather a systematic presentation and evaluation of commonalities and specifics of higher order approaches and tools, with an eye toward their practical applicability and usefulness. Moreover, the focus is on techniques in the frequency domain. The paper is organized as follows. Section II presents different higher order IE and DE formulations. This includes SIE formulations for structures made from a perfect electric conductor (PEC) and arbitrary material structures, respectively, VIE and VSIE formulations, SIE-Green's function formulations for multilayer structures, hybrid MoM-physical optics (PO) formulations, and FEM formulations with different hybridizations. In Section III, most frequently used surface and volume elements for higher order geometrical modeling in CEM are reviewed, including generalized curved parametric quadrilaterals, triangles, hexahedra, and tetrahedra. Section IV discusses higher order current and field modeling using different types of hierarchical and interpolatory vector basis functions, in both divergence- and curl-conforming arrangements, on different higher order geometrical elements from the previous section. Higher order spatial/temporal basis functions for time-domain techniques are also presented. Section V addresses various components of higher order solutions, such as testing procedures, evaluation of singular integrals, Nyström discretization, acceleration using the multilevel fast multipole algorithm (MLFMA) and plane-wave time-domain (PWTD) algorithm, matrix solvers, error estimates, adaptive schemes, and mesh generation. In Section VI, the accuracy, convergence, and efficiency of higher order CEM techniques, and their advantages over low-order solutions, are demonstrated and evaluated in several characteristic examples.

II. Higher Order IE and DE Formulations

A. Higher Order SIE Formulations for PEC Structures

Surface integral equations (SIEs) for three-dimensional (3-D) PEC structures, with the surface electric current density vector, $\mathbf{J}_{\mathrm{s}}$, as unknown quantity, are based on boundary conditions for the total (incident plus scattered) electromagnetic field on the surface of the structure (S). In particular, for the analysis in the frequency domain, the boundary condition for the tangential component of the total electric field intensity vector yields the electric field integral equation (EFIE)

$$\eta_{\mathrm{e}}\mathbf{n}\times\mathbf{L}_{\mathrm{e}}^{(\mathrm{s})}(\mathbf{J}_{\mathrm{s}})=\mathbf{n}\times\mathbf{E}^{\mathrm{inc}},\quad \eta_{\mathrm{e}}=\sqrt{\frac{\mu_{\mathrm{e}}}{\varepsilon_{\mathrm{e}}}} \tag{1}$$

whereas the magnetic field integral equation (MFIE), expressing the boundary condition for the total magnetic field intensity vector, reads

$$\mathbf{n}\times\mathbf{K}_{\mathrm{e}}^{(\mathrm{s})}(\mathbf{J}_{\mathrm{s}})+\frac{1}{2}\mathbf{J}_S=\mathbf{n}\times\mathbf{H}^{\mathrm{inc}}. \tag{2}$$

$\mathbf{E}^{\mathrm{inc}}$ and $\mathbf{H}^{\mathrm{inc}}$ are, respectively, incident electric and magnetic field intensity vectors, $\mathbf{n}$ is the outward unit normal on S, and ε_{e}, μ_{e}, and η_{e} are the complex permittivity, permeability, and intrinsic impedance of the external homogeneous medium around

the structure (most frequently free space). The integral operators $\mathbf{L}^{(\mathrm{s})}$ and $\mathbf{K}^{(\mathrm{s})}$ are defined as

$$\mathbf{L}^{(\mathrm{s})}(\mathbf{J}_\mathrm{s}) = \mathrm{j}k \int_S \left(\mathbf{J}_\mathrm{s} g + \frac{1}{k^2} \nabla_\mathrm{s} \cdot \mathbf{J}_\mathrm{s} \nabla g \right) \mathrm{d}S$$
$$\mathbf{K}^{(\mathrm{s})}(\mathbf{J}_\mathrm{s}) = \int_S \mathbf{J}_\mathrm{s} \times \nabla g \mathrm{d}S, \quad g = \frac{\mathrm{e}^{-jkR}}{4\pi R}, \quad k = \omega\sqrt{\varepsilon\mu} \quad (3)$$

with g and k denoting Green's function and wave number, respectively, for the unbounded medium of parameters $\varepsilon = \varepsilon_\mathrm{e}$ and $\mu = \mu_\mathrm{e}$, R the distance of the field point from the source point, and ω the angular frequency. The integral $\mathbf{K}^{(\mathrm{s})}$ is computed in the principal value sense. Either one of (1) and (2) can be used independently to solve for $\mathbf{J}_\mathrm{s}$, with the EFIE being used much more frequently, primarily because the MFIE cannot handle open metallic surfaces (e.g., thin wires and plates). In the case of metallic surfaces with distributed loadings, e.g., surfaces with resistive or dielectric layers (coatings), conductors with skin effect taken into account, etc., a self-term $Z_\mathrm{s}\mathbf{J}_\mathrm{s}$ is incorporated in (1), where Z_s is the appropriate surface impedance. In the case of thin metallic wires, $\mathbf{J}_\mathrm{s}$ becomes the line current intensity, I, along the generatrices of wires (the reduced-kernel approximation for wires), and integrals over S in (3) reduce to line integrals. Higher order solutions to the EFIE are presented in [2]–[4], [24], [25], [29]–[34], [36]–[45], [49]–[51], [54]–[56], [58], and [59], and solutions to the MFIE in [4], [23], [24], [30], [33], [35], [37], [44], [49], [50], [55], [56], and [58].

In analysis of closed metallic structures (i.e., if S is a closed surface) in a lossless external medium, both EFIE and MFIE formulations suffer from internal resonance problems, associated with spurious solutions at resonant frequencies of a cavity formed by filling the interior of S with the external medium. One approach to overcome these problems is to linearly combine (1) and (2) together to form the combined field integral equation (CFIE)

$$\alpha\eta_\mathrm{e}\mathbf{n} \times \left[\mathbf{L}_\mathrm{e}^{(\mathrm{s})}(\mathbf{J}_\mathrm{s}) \times \mathbf{n} \right] + (1-\alpha)\eta_\mathrm{e} \left[\mathbf{n} \times \mathbf{K}_\mathrm{e}^{(\mathrm{s})}(\mathbf{J}_\mathrm{s}) + \frac{1}{2}\mathbf{J}_\mathrm{s} \right] = \alpha\mathbf{n} \times \left(\mathbf{E}^\mathrm{inc} \times \mathbf{n} \right) + (1-\alpha)\eta_\mathrm{e}\mathbf{n} \times \mathbf{H}^\mathrm{inc}. \quad (4)$$

Numerical experiments show that the choice of the combination parameter α is not critical for the analysis; it is usually adopted as $\alpha = 0.5$, which would put the same weight on the electric and magnetic fields in the equation if they were those of a uniform plane wave ($E/H = \eta_\mathrm{e}$). The CFIE is discretized to higher orders in [3], [24], [31], [45], [49], [50], [55], and [56].

For transient SIE analysis of PEC structures, time-domain integral equations (TDIEs) analogous to those in (1)–(4), namely, TD-EFIE, TD-MFIE, and TD-CFIE formulations, are used [53]. In TDIE models, the given IE is discretized in both space, over S, and time. TD formulations enable effective modeling of time-varying and nonlinear problems and fast broadband simulations (provide broadband information in a single run), at the expense of the additional discretization – in time domain.

B. Higher Order SIE Formulations for Arbitrary Material Structures

In SIE formulations for arbitrary 3-D material structures, we use the surface equivalence principle (generalized Huygens' principle) to break the entire structure into substructures, each representing one of the homogeneous dielectric regions (domains) constituting the structure, together with the belonging metallic surfaces, with the remaining space being filled with the same medium (of that region). One of the domains is the external space surrounding the structure. The scattered electric and magnetic fields in each domain can be expressed in terms of the equivalent surface electric and magnetic currents, of densities $\mathbf{J}_\mathrm{s}$ and $\mathbf{M}_\mathrm{s}$, which are placed on the boundary surface of the domain, with the objective to produce a zero total field in the remaining space. These current densities are given by the following boundary conditions:

$$\mathbf{J}_\mathrm{s} = \mathbf{n} \times \mathbf{H}^\mathrm{tot}, \quad \mathbf{M}_\mathrm{s} = -\mathbf{n} \times \mathbf{E}^\mathrm{tot} \quad (5)$$

where $\mathbf{E}^\mathrm{tot}$ and $\mathbf{H}^\mathrm{tot}$ are the total electric and magnetic field intensities at the boundary surface just inside the domain, and $\mathbf{n}$ is the unit normal on the surface directed into the domain. On the metallic surfaces, only the surface electric currents ($\mathbf{J}_\mathrm{s}$) exist. For the boundary surface between any two adjacent dielectric domains (domains p and q), we write separately the boundary conditions (5) for the two domains (with a zero field outside), and then combine them together, with the expressions for domain q multiplied by parameters α and β. This leads to [3]

$$\begin{aligned} \mathbf{n}_{pq} \times & \left\{ \left[\eta_p \mathbf{L}_p^{(\mathrm{s})}(\mathbf{J}_\mathrm{s}) - \mathbf{K}_p^{(\mathrm{s})}(\mathbf{M}_\mathrm{s}) \right] \right. \\ & \left. -\alpha \left[\eta_q \mathbf{L}_q^{(\mathrm{s})}(-\mathbf{J}_\mathrm{s}) - \mathbf{K}_q^{(\mathrm{s})}(-\mathbf{M}_\mathrm{s}) \right] \right\} \\ & - \frac{1}{2}(1-\alpha)\mathbf{M}_\mathrm{s} \\ = & \mathbf{n}_{pq} \times \left(\mathbf{E}_p^\mathrm{inc} - \alpha \mathbf{E}_q^\mathrm{inc} \right) \quad (6) \end{aligned}$$

$$\begin{aligned} & \mathbf{n}_{pq} \times \left\{ \left[\mathbf{K}_p^{(\mathrm{s})}(\mathbf{J}_\mathrm{s}) + \eta_p^{-1} \mathbf{L}_p^{(\mathrm{s})}(\mathbf{M}_\mathrm{s}) \right] \right. \\ & \left. -\beta \left[\mathbf{K}_q^{(\mathrm{s})}(-\mathbf{J}_\mathrm{s}) + \eta_q^{-1} \mathbf{L}_q^{(\mathrm{s})}(-\mathbf{M}_\mathrm{s}) \right] \right\} \\ & + \frac{1}{2}(1-\beta)\mathbf{J}_\mathrm{s} \\ = & \mathbf{n}_{pq} \times \left(\mathbf{H}_p^\mathrm{inc} - \beta \mathbf{H}_q^\mathrm{inc} \right) \quad (7) \end{aligned}$$

which is a set of coupled SIEs (EFIE and MFIE) with $\mathbf{J}_\mathrm{s}$ and $\mathbf{M}_\mathrm{s}$ as unknown quantities. The operators $\mathbf{L}_p$ and $\mathbf{K}_p$, (3), are computed on the boundary surface just inside domain p, using material parameters of that domain (ε_p and μ_p), $\mathbf{L}_q$ and $\mathbf{K}_q$ are computed on the other side of the surface, using material parameters of domain q (ε_q and μ_q), and $\mathbf{n}_{pq}$ is directed from domain q to domain p. Similarly, $(\mathbf{E}_p^\mathrm{inc}, \mathbf{H}_p^\mathrm{inc})$ and $(\mathbf{E}_q^\mathrm{inc}, \mathbf{H}_q^\mathrm{inc})$ represent the fields due to the impressed sources in domains p and q, respectively, assumed to radiate as if in an unbounded medium of parameters (ε_p, μ_p) or (ε_q, μ_q) and computed at the same locations as the corresponding scattered fields. For example, if domain p is the external space from which a plane electromagnetic wave illuminates the structure, $(\mathbf{E}_p^\mathrm{inc}, \mathbf{H}_p^\mathrm{inc})$ is the field of the wave and $\mathbf{E}_q^\mathrm{inc}$, $\mathbf{H}_q^\mathrm{inc} = 0$, whereas $\mathbf{E}_p^\mathrm{inc}$, $\mathbf{H}_p^\mathrm{inc} = 0$ if, as another example, the generator feeding an antenna via its field $(\mathbf{E}_q^\mathrm{inc}, \mathbf{H}_q^\mathrm{inc})$ resides in domain q. Note that the factors 1/2 in the last terms on the left-hand side of both (6) and (7) signify the fact that the integral $\mathbf{K}^{(\mathrm{s})}$ in (3) is evaluated in the principal value sense. Otherwise, these terms would be $-(1-\alpha)\mathbf{M}_\mathrm{s}$ and $(1-\beta)\mathbf{J}_\mathrm{s}$ [57], the difference coming from the quasistatic

self-fields near the surface, given by $(\mathbf{E}_p)_{\rm self} = \mathbf{n}_{pq} \times \mathbf{M}_{\rm s}/2$ and $(\mathbf{H}_p)_{\rm self} = -\mathbf{n}_{pq} \times \mathbf{J}_{\rm s}/2$ on the side toward domain p, and $(\mathbf{E}_q)_{\rm self} = -(\mathbf{E}_p)_{\rm self}$ and $(\mathbf{H}_q)_{\rm self} = -(\mathbf{H}_p)_{\rm self}$ on the other side of the surface, which are not included in $\mathbf{K}^{(\rm s)}$.

Depending on the choice of α and β in (6) and (7), different SIE formulations are obtained for this problem. The most frequently used formulation, with higher order solutions in [3], [40]–[43], [52], [57], is the Poggio, Miller, Chang, Harrington, Wu, and Tsai (PMCHWT) formulation, adopting $\alpha = \beta = 1$. This eliminates the terms proportional to $\mathbf{M}_{\rm s}$ and $\mathbf{J}_{\rm s}$ in (6) and (7), respectively, and is equivalent to putting the same weight, in the respective equations, on the total electric/magnetic fields at the two sides of the boundary. Müller's formulation, implemented in [56], [57] with a higher order discretization, specifies $\alpha = -\varepsilon_q/\varepsilon_p$ and $\beta = -\mu_q/\mu_p$, which eliminates the quasistatic electric and magnetic fields due to electric and magnetic charges associated with $\mathbf{J}_{\rm s}$ and $\mathbf{M}_{\rm s}$, respectively, in (6) and (7), and thus effectively reduces the order of singularity of equations. This, in turn, facilitates the integration involved in computing MoM matrix elements and improves the conditioning properties of the equations. However, Müller's formulation leads to inaccuracies in the solution for high-contrast material structures and for structures with geometrical singularities (e.g., edge singularities) [57].

C. Higher Order VIE Formulations

Employing the volume equivalence principle, an inhomogeneous (possibly lossy) dielectric structure, of complex permittivity $\varepsilon_{\rm i}$, surrounded by a homogeneous medium of complex permittivity $\varepsilon_{\rm e}$ ($\mu_{\rm i} = \mu_{\rm e}$), which most frequently is free space ($\varepsilon_{\rm e} = \varepsilon_0$, $\mu_{\rm e} = \mu_0$), can be represented by a system of equivalent volume electric (polarization and conduction) currents, of density $\mathbf{J}$, radiating in an unbounded medium of parameters $\varepsilon_{\rm e}$ and $\mu_{\rm e}$. From the constitutive equation for these currents (generalized local Ohm's law), $\mathbf{J}$ is related to the total electric field intensity, $\mathbf{E}^{\rm tot}$, at any point in the dielectric as $\mathbf{J} = \sigma_{\rm E}\mathbf{E}^{\rm tot}$, with $\sigma_{\rm E} = {\rm j}\omega(\varepsilon_{\rm i} - \varepsilon_{\rm e})$ being the equivalent electric conductivity at that point. This gives the following volume integral equation (VIE), with $\mathbf{J}$ as unknown quantity:

$$\frac{\mathbf{J}}{{\rm j}\omega(\varepsilon_{\rm i} - \varepsilon_{\rm e})} + \eta_{\rm e}\mathbf{L}_{\rm e}^{(v)}(\mathbf{J}) = \mathbf{E}^{\rm inc} \tag{8}$$

where the integral operator $\mathbf{L}^{(v)}$ is the volumetric version, with integration over the volume (V) of the dielectric structure, of that in (3). If divergence-conforming bases are used in the VIE model, $\mathbf{J}$ in (8) is expressed in terms of the electric flux density vector, $\mathbf{D}$, whose normal component is continuous across the surfaces with abrupt changes of dielectric parameters. The relationship between the two vectors is

$$\mathbf{J} = {\rm j}\omega K\mathbf{D}, \quad K = \frac{\varepsilon_{\rm i} - \varepsilon_{\rm e}}{\varepsilon_{\rm i}} \tag{9}$$

where K stands for the electric contrast of the dielectric with respect to the external (background) medium. Higher order solutions to the VIE are those in [68]–[77].

A dual VIE to that in (8) can be written for the equivalent volume magnetic current density, $\mathbf{M}$, throughout the volume of an inhomogeneous magnetic structure based on the constitutive equation with the equivalent magnetic conductivity, $\sigma_{\rm H} = {\rm j}\omega(\mu_{\rm i} - \mu_{\rm e})$, at a point as a proportionality constant. For materials with both dielectric (including conducting) and magnetic properties, a set of two coupled VIEs with both $\mathbf{J}$ and $\mathbf{M}$ as unknown quantities is solved. Finally, for anisotropic materials, VIEs with tensor permittivity and/or permeability can be used.

D. Higher Order VSIE Formulations

In addition to using the general SIE formulation in (6) and (7), analysis of structures composed of both dielectric and PEC parts can be performed combining the VIE for dielectric structures in (8) and surface EFIE for PEC structures in (1). The resulting hybrid VIE-SIE or VSIE formulation, given by

$$\begin{aligned} \frac{\mathbf{J}}{{\rm j}\omega(\varepsilon_{\rm i} - \varepsilon_{\rm e})} + \eta_{\rm e}\left[\mathbf{L}_{\rm e}^{(v)}(\mathbf{J}) + \mathbf{L}_{\rm e}^{(\rm s)}(\mathbf{J}_{\rm s})\right] &= \mathbf{E}^{\rm inc} \\ \eta_{\rm e}\mathbf{n} \times \left[\mathbf{L}_{\rm e}^{(v)}(\mathbf{J}) + \mathbf{L}_{\rm e}^{(\rm s)}(\mathbf{J}_{\rm s})\right] &= \mathbf{n} \times \mathbf{E}^{\rm inc} \end{aligned} \tag{10}$$

solves simultaneously for $\mathbf{J}$ throughout the dielectric domains (V) and $\mathbf{J}_{\rm s}$ over the PEC surfaces (S) of the composite structure, with higher order discretizations in [41] and [78].

Moreover, VIE discretization can be added to the SIE system in (6) and (7) to account for inhomogeneous parts of the structure. For instance, if homogeneous material domain q in a SIE model with the PMCHWT ($\alpha = \beta = 1$) version of (6) and (7) encloses an inhomogeneous dielectric object of permittivity $\varepsilon_{\rm i}$, which is treated by the VIE in (8), the hybrid VSIE system of equations reads

$$\begin{aligned} \mathbf{n}_{pq} \times &\left[\mathbf{E}_p^{\rm inc} - \eta_p\mathbf{L}_p^{(\rm s)}(\mathbf{J}_{\rm s}) + \mathbf{K}_p^{(\rm s)}(\mathbf{M}_{\rm s})\right] \\ &= \mathbf{n}_{pq} \times \Big[\mathbf{E}_q^{\rm inc} - \eta_q\mathbf{L}_q^{(\rm s)}(-\mathbf{J}_{\rm s}) \\ &\quad + \mathbf{K}_q^{(\rm s)}(-\mathbf{M}_{\rm s}) - \eta_q\mathbf{L}_q^{(v)}(\mathbf{J})\Big] \end{aligned} \tag{11}$$

$$\begin{aligned} \mathbf{n}_{pq} \times &\left[\mathbf{H}_p^{\rm inc} - \mathbf{K}_p^{(\rm s)}(\mathbf{J}_{\rm s}) - \eta_p^{-1}\mathbf{L}_p^{(\rm s)}(\mathbf{M}_{\rm s})\right] \\ &= \mathbf{n}_{pq} \times \Big[\mathbf{H}_q^{\rm inc} - \mathbf{K}_q^{(\rm s)}(-\mathbf{J}_{\rm s}) \\ &\quad - \eta_q^{-1}\mathbf{L}_q^{(\rm s)}(-\mathbf{M}_{\rm s}) - \mathbf{K}_q^{(v)}(\mathbf{J})\Big] \end{aligned} \tag{12}$$

$$\begin{aligned} &\frac{\mathbf{J}}{{\rm j}\omega(\varepsilon_{\rm i} - \varepsilon_q)} + \eta_q\mathbf{L}_q^{(\rm s)}(-\mathbf{J}_{\rm s}) \\ &\quad - \mathbf{K}_q^{(\rm s)}(-\mathbf{M}_{\rm s}) + \eta_q\mathbf{L}_q^{(v)}(\mathbf{J}) = \mathbf{E}_q^{\rm inc}. \end{aligned} \tag{13}$$

Its higher order solutions are presented in [79] and [9].

E. Higher Order SIE-Green's Function Formulations for Multilayer Structures

IE formulations aimed to dealing with arbitrarily shaped composite metallic and dielectric structures, such as the SIE formulation in (6) and (7), and VSIE formulations in (10) and (11)–(13), respectively, cannot be regarded as an optimal solution to problems involving PEC structures in planar multilayer dielectric media (e.g., multilayer microstrip antennas and circuits). Simply, most of unknowns in a model are employed for modeling the dielectric layers, which is rather uneconomical for problems where layers can be treated as of infinite extent. Here, significant advancements in efficiency and accuracy of

the analysis can be achieved by combining the SIE approach to the analysis of PEC structures (in a homogeneous environment) with exact Green's functions for an infinite multilayer dielectric medium. An example is the EFIE in (1) with $\mathbf{L}^{(\mathrm{s})}$ transformed from the expression in (3) to the following mixed-potential form (MPIE) for multilayer environments [51], [59]:

$$\mathbf{L}^{(\mathrm{s})}(\mathbf{J}_\mathrm{s}) = \mathrm{j}k \int_S \underline{\underline{\mathbf{G}}}^A \cdot \mathbf{J}_\mathrm{s} \mathrm{d}S + \frac{1}{k^2} \nabla \int_S G^\Phi \nabla_\mathrm{s} \cdot \mathbf{J}_\mathrm{s} \mathrm{d}S \quad (14)$$

where $\underline{\underline{\mathbf{G}}}^A$ is the dyadic Green's function for the magnetic vector potential, $\mathbf{A}$, in the layered medium, G^Φ is the corresponding scalar Green's function for the electric scalar potential, Φ, and $\mathbf{J}_\mathrm{s}$ is the electric surface current density over PEC surfaces in the model, which is the only unknown quantity for the problem. Equations (1) and (14) thus represent an SIE-Green's function formulation for analysis of PEC structures of arbitrary shapes immersed in arbitrary multilayer media. It is implemented using higher order surface elements and basis functions in [51], [59]. Other MPIE formulations are also possible, with different forms of the associated dyadic Green's functions [132].

F. Higher Order MoM-PO Formulations

One strategy to substantially enhance the efficiency of MoM solutions at high frequencies is based on its hybridization with high-frequency techniques for asymptotic analysis of electrically very large smooth parts of the structure. A notable example are current-based hybrid rigorous-asymptotic techniques combining MoM and physical optics (PO). In a MoM-PO model, the structure under consideration is decomposed into two parts, a MoM region, with currents $\mathbf{J}_\mathrm{s}^{\mathrm{MoM}}$, and a PO region, with currents $\mathbf{J}_\mathrm{s}^{\mathrm{PO}}$, so that the total currents over the structure surface can be written as

$$\mathbf{J}_\mathrm{s} = \mathbf{J}_\mathrm{s}^{\mathrm{MoM}} + \mathbf{J}_\mathrm{s}^{\mathrm{PO}}. \quad (15)$$

Theoretical foundation of the hybrid technique is a system of coupled SIEs (1) and (2), with the EFIE in the MoM region and MFIE in the PO region. In (2), the PO approximation for surface currents is employed, which inherently neglects mutual interaction effects within the currents in the asymptotic region and imposes the geometrical-optics shadow condition, thus reducing the MFIE to

$$\begin{aligned} \mathbf{n} \times \mathbf{K}_\mathrm{e}^{(\mathrm{s})}(\mathbf{J}_\mathrm{s}^{\mathrm{MoM}}) + \frac{1}{2}\mathbf{J}_\mathrm{s}^{\mathrm{PO}} \\ = \mathbf{n} \times \mathbf{H}^{\mathrm{inc}} \quad (\text{in the lit PO region}) \\ \mathbf{J}_\mathrm{s}^{\mathrm{PO}} = 0 \quad (\text{in the shadowed PO region}). \end{aligned} \quad (16)$$

Higher order solutions are given in [44] and [46].

G. Higher Order FEM Formulations

Higher order FEM techniques for electromagnetic modeling of inhomogeneous material structures are based on volumetric discretizations of the curl-curl electric-field vector wave equation (E-field FEM formulation)

$$\begin{aligned} \nabla \times \mu_\mathrm{r}^{-1} \nabla \times \mathbf{E} - k_0^2 \varepsilon_\mathrm{r} \mathbf{E} = -\mathrm{j}k_0 \eta_0 \mathbf{J}_\mathrm{i} - \nabla \times \mu_\mathrm{r}^{-1} \mathbf{M}_\mathrm{i} \\ k_0 = \omega \sqrt{\varepsilon_0 \mu_0} \end{aligned} \quad (17)$$

where ε_r and μ_r are complex relative permittivity and permeability of the medium (tensors for anisotropic materials), $\mathbf{J}_\mathrm{i}$ and $\mathbf{M}_\mathrm{i}$ are impressed electric and magnetic current densities, and $\mathbf{E}$ is the total electric field intensity vector – the unknown quantity to be determined in a solution procedure. At material interfaces, $\mathbf{E}$ must be tangentially continuous. The curl-curl magnetic-field vector wave equation, with the total magnetic field intensity vector, $\mathbf{H}$, as unknown quantity (H-field formulation), can be written in a dual fashion.

Using the Galerkin testing procedure, the weak form representation of (17) suitable for numerical solution can be written as

$$\begin{aligned} \int_V \mu_\mathrm{r}^{-1} (\nabla \times \mathbf{w}) \cdot (\nabla \times \mathbf{E}) \, \mathrm{d}V - k_0^2 \int_V \varepsilon_\mathrm{r} \mathbf{w} \cdot \mathbf{E} \, \mathrm{d}V \\ = -\int_V (\mathrm{j}k_0 \eta_0 \mathbf{w} \cdot \mathbf{J}_\mathrm{i} + \nabla \times \mu_\mathrm{r}^{-1} \mathbf{M}_\mathrm{i}) \mathrm{d}V \\ + \mathrm{j}k_0 \eta_0 \oint_S \mathbf{w} \cdot (\mathbf{n} \times \mathbf{H}) \mathrm{d}S \end{aligned} \quad (18)$$

where V and S are, respectively, the volume and boundary surface of the FEM computational region, and $\mathbf{w}$ is a testing function. Higher order discretizations of the FEM region for the frequency-domain analysis can be found in [25], [82]–[96], [98]–[113], and [115]–[119], and those for the time-domain analysis in [97] and [114]. The tangential component of $\mathbf{H}$ over S is determined by the appropriate boundary conditions imposed at the surface, providing a foundation for a numerical interface between the FEM domain and the remaining space for modeling of unbounded problems (e.g., antennas and scatterers), i.e., for implementing mesh termination schemes based on absorbing boundary conditions (ABCs) [93] and boundary integral (BI) equations [9], [85], [93]–[97], [117], leading to different versions of hybrid FEM methodologies.

FEM-ABC techniques impose approximate local conditions across the faces of finite elements associated with the outer boundary S of the FEM region, thus simulating the zero-reflection conditions of the open space and enabling the mesh termination, while preserving the simplicity of the FEM method and sparsity of the final system. However, as the solution obtained by an ABC is approximate, the truncation surface (S) must be placed sufficiently far away from the material structure and must have a convex shape, which significantly increases the computational domain. The BI terminations are exact, and hence S can be placed as close to the structure as possible and can take an arbitrary shape. However, the FE-BI method leads to matrices that are not purely sparse, but sparse with fully populated sub-blocks (BI blocks), which increases computational complexity of the hybrid solution.

H. Higher Order FE-BI Formulations

In higher order FE-BI techniques for unbounded problems [9], [85], [93]–[96], the FEM region V in (18) is truncated and numerically closed (completed) by SIE (MoM) solution outside V. The SIE formulation thus provides exact boundary conditions in terms of boundary integrals for the FEM region. If, with reference to the notation in (6) and (7), material domain q belongs to the FEM region in the model, while domain p is in the external region, boundary conditions (5) at the boundary surface

between the two domains, just outside domain q, give the following EFIE and MFIE:

$$\mathbf{n}_{pq}\times\left[\eta_p\mathbf{L}_p^{(\mathrm{s})}(\mathbf{J}_\mathrm{s})-\mathbf{K}_p^{(\mathrm{s})}(\mathbf{M}_\mathrm{s})\right]-\frac{1}{2}\mathbf{M}_\mathrm{s}=\mathbf{n}_{pq}\times\mathbf{E}_p^{\mathrm{inc}}, \quad (19)$$

$$\mathbf{n}_{pq}\times\left[\mathbf{K}_p^{(\mathrm{s})}(\mathbf{J}_\mathrm{s})+\eta_p^{-1}\mathbf{L}_p^{(\mathrm{s})}(\mathbf{M}_\mathrm{s})\right]+\frac{1}{2}\mathbf{J}_\mathrm{s}=\mathbf{n}_{pq}\times\mathbf{H}_p^{\mathrm{inc}}. \quad (20)$$

These equations, coupled through

$$\mathbf{M}_\mathrm{s}=\mathbf{E}_q\times\mathbf{n}_{pq} \quad (21)$$

to the FEM solution for the electric field intensity $\mathbf{E}_q$ in domain q using (18), constitute a FE-BI formulation with $\mathbf{E}$ in the FEM region and $\mathbf{J}_\mathrm{s}$ and $\mathbf{M}_\mathrm{s}$ over the BI surface as unknown quantities. To avoid internal resonance problems, (19) and (20) can be combined to form a CFIE, as in (4).

In [97], an efficient higher order FE-BI hybridization in time domain (TD-FE-BI) is obtained via the first-order impedance boundary condition on S, leading to the following functional for the boundary value problem:

$$\begin{aligned}F(\mathbf{E})&=\frac{1}{2}\int_V\left[\mu_\mathrm{r}^{-1}(\nabla\times\mathbf{E})\cdot(\nabla\times\mathbf{E})+\mu_0\varepsilon\,\partial_\mathrm{t}^2\mathbf{E}\cdot\mathbf{E}+\mu_0\sigma\,\partial_\mathrm{t}\mathbf{E}\cdot\mathbf{E}\right]\mathrm{d}V\\&\quad+\frac{1}{2}\oint_S\left[c^{-1}\partial_\mathrm{t}(\mathbf{n}\times\mathbf{E})\cdot(\mathbf{n}\times\mathbf{E})+2\mathbf{E}\cdot\mathbf{U}_\mathrm{s}\right]\mathrm{d}S\end{aligned} \quad (22)$$

whose stationary point is the solution to the problem, where $c=1/\sqrt{\varepsilon_0\mu_0}$ is the velocity of electromagnetic waves in free space and U_s is an unknown function on S evaluated using a BI in terms of equivalent electric and magnetic surface currents, $\mathbf{J}_\mathrm{s}$ and $\mathbf{M}_\mathrm{s}$, placed on a closed surface S_0 that resides inside S but fully encloses the material structure. With the BI term neglected, the impedance boundary condition imposed in (22) becomes the first-order ABC (which ensures zero reflection only for the normally incident waves). The BI thus corrects the first-order ABC such that (22) essentially provides an exact ABC. On the other side, the hybridization in (22) preserves the sparsity of the FE matrix (like FEM-ABC hybridizations) and its solution is free of spurious modes associated with internal BI resonances, since the impedance boundary condition prevents any real resonance in the cavity formed by S.

III. Higher Order Geometrical Modeling

A. Generalized Curved Parametric Quadrilaterals

An arbitrary surface can be represented by a mesh with a basic building element in the form of a generalized curved parametric quadrilateral defined by the following equation in two parametric coordinates (u and v):

$$\mathbf{r}=\mathbf{r}(u,v),\quad -1\le u,v\le 1 \quad (23)$$

where $\mathbf{r}$ is the position vector (with respect to the global coordinate origin) of the point determined by parameters u and v on the quadrilateral surface. The quadrilateral surface is bounded by lines $u=\pm1$ and $v=\pm1$. Equation (23) defines a parametric transformation (mapping) from a square parent domain in a local parametric u-v coordinate system to a curved quadrilateral in the global 3-D (x-y-z) coordinate system, and vice versa, as illustrated in Fig. 1. The function $\mathbf{r}(u,v)$ is sometimes known exactly, as an analytical expression for a given surface (e.g., a part of the surface of a sphere [2]). Most frequently, it is approximated using a double sum of two-dimensional power functions

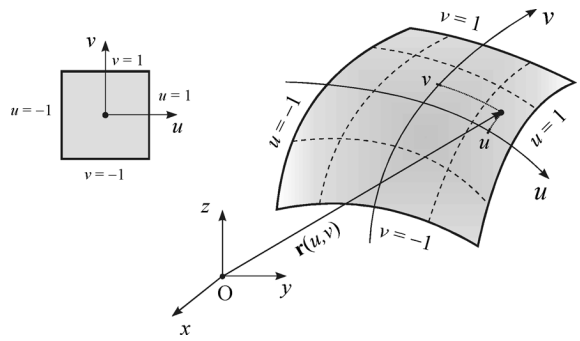

Fig. 1. Generalized curved parametric quadrilateral defined by (23); Square parent domain is also shown.

$$\mathbf{r}(u,v)=\sum_{m=0}^{K_u}\sum_{n=0}^{K_v}\mathbf{b}_{mn}u^m v^n \quad (24)$$

where K_u and K_v (K_u, $K_v\ge1$) are adopted (theoretically arbitrarily high) geometrical orders of the element along the u- and v-parametric coordinate, respectively, and $\mathbf{b}_{mn}$ are constant vector coefficients to be determined. The simplest way to determine these coefficients is to require that a total of $M=(K_u+1)(K_v+1)$ points, (u_m,v_n) for $0\le m\le K_u$, $0\le n\le K_v$, of the parametric quadrilateral (interpolation nodes) belong to the actual surface that is being approximated, which results in

$$\mathbf{r}(u,v)=\sum_{m=0}^{K_u}\sum_{n=0}^{K_v}\mathbf{r}_{mn}L_m^{K_u}(u)L_n^{K_v}(v). \quad (25)$$

Here, $\mathbf{r}_{mn}=\mathbf{r}(u_m,v_n)$ are position vectors of interpolation nodes and $L_m^{K_u}$ represent Lagrange interpolation polynomials given by

$$L_m^{K_u}(u)=\prod_{\substack{j=0\\ j\ne m}}^{K_u}\frac{u-u_j}{u_m-u_j} \quad (26)$$

with u_j being the interpolation nodes along an interval $-1\le u\le1$ (note that $L_m^{K_u}$ is unity for $u=u_m$ and zero at all other nodes), and similarly for $L_n^{K_v}(v)$. Usually, the equidistant distribution of interpolation nodes along each coordinate in the parametric space is used. Of course, the use of specific non-equidistant node distributions, which would provide additional modeling flexibility and accuracy in some applications, is possible as well.

Fig. 2(a) shows the simplest Lagrange generalized quadrilateral, defined by $K_u=K_v=1$ in (25) and called the bilinear quadrilateral. It is determined solely by $M=4$ interpolation points – its 4 vertices (arbitrarily positioned in space), so that (25) and (24) become

$$\begin{aligned}\mathbf{r}(u,v)&=\frac{1}{4}[\mathbf{r}_{00}(1-u)(1-v)+\mathbf{r}_{10}(u+1)(1-v)\\&\quad+\mathbf{r}_{01}(1-u)(v+1)+\mathbf{r}_{11}(u+1)(v+1)]\\&=\mathbf{b}_{00}+\mathbf{b}_{10}u+\mathbf{b}_{01}v+\mathbf{b}_{11}uv.\end{aligned} \quad (27)$$

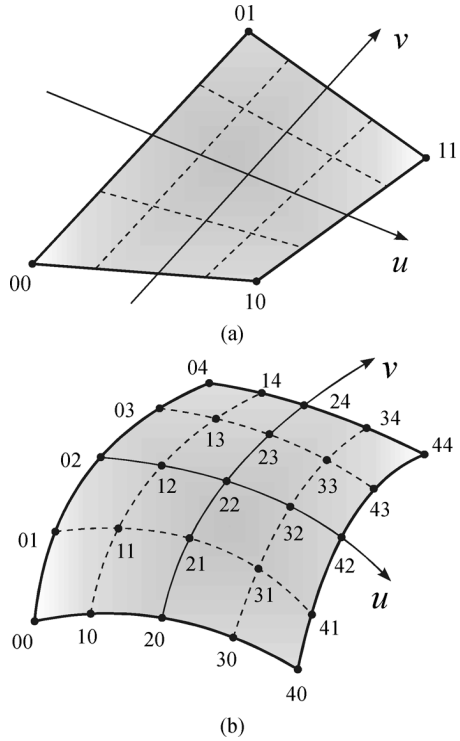

Fig. 2. Examples of Lagrange generalized quadrilaterals in (25): (a) bilinear quadrilateral in (27) and (b) quadrilateral of the fourth geometrical order in (28).

Its edges and all coordinate lines are straight, while its surface is somewhat curved (inflexed). As another example, the quadrilateral of the fourth geometrical order ($K_u = K_v = 4$, $M = 25$), assuming the uniform distribution of interpolation nodes in the square parent domain, is given by

$$\begin{aligned}\mathbf{r}(u,v) &= \frac{4}{9}\mathbf{r}_{00}(u+0.5)u(u-0.5)(u-1)(v+0.5)\\ &\quad\cdot v(v-0.5)(v-1)\\ &\quad-\frac{16}{9}\mathbf{r}_{10}(u+1)u(u-0.5)(u-1)(v+0.5)\\ &\quad\cdot v(v-0.5)(v-1)+\cdots\\ &\quad+\frac{4}{9}\mathbf{r}_{44}(u+1)(u+0.5)\\ &\quad\cdot u(u-0.5)(v+1)(v+0.5)v(v-0.5)\\ &= \mathbf{b}_{00}+\mathbf{b}_{10}u+\mathbf{b}_{20}u^2+\mathbf{b}_{30}u^3+\mathbf{b}_{40}u^4\\ &\quad+\cdots+\mathbf{b}_{04}v^4+\mathbf{b}_{14}uv^4\\ &\quad+\mathbf{b}_{24}u^2v^4+\mathbf{b}_{34}u^3v^4+\mathbf{b}_{44}u^4v^4 \qquad (28)\end{aligned}$$

and depicted in Fig. 2(b). Of course, for modeling of cross sections of arbitrary cylindrical structures (in FEM or MoM-VIE 2-D techniques), only planar (2-D) curvilinear quadrilaterals of the form in (24) or (25) are used (all the interpolation nodes in Figs. 1 and 2 belong to the cross-section considered).

Note that, in general, the surface tangent is discontinuous on the boundary of two attached curved Lagrange quadrilateral elements, defined by (25), regardless of the geometrical orders K_u and K_v of the quadrilaterals. However, this geometrical discontinuity across the boundaries of adjacent elements becomes less pronounced as the elements of higher geometrical orders are used. For instance, when approximating a circular cylinder using 32 interpolation points along its circumference and three different geometrical models constructed from (A) 32 first-order ($K_u = K_v = 1$) elements, (B) 16 second-order ($K_u = K_v = 2$) elements, and (C) 8 fourth-order ($K_u = K_v = 4$) elements per cylinder circumference, the angles between the surface tangents of the neighboring elements at the junctions in models (A), (B), and (C) are 168.750°, 179.787°, and 180.011°, respectively, compared to the exact 180° [43]. If a more accurate model is needed, one can increase the total number and/or geometrical orders of patches.

On the other side, more complicated parametric quadrilateral surfaces that provide continuous surface tangents across the edges shared by curved elements can be used. In one dimension (i.e., along each parametric line), these higher order geometrical approximations take into account not only the values of the function that is being interpolated, but also the values of its first derivative (or even higher order derivatives, in general). For example, third-order (cubic) B-splines (or beta-splines) [133] ensure the continuity of the function and its first and second derivatives at the endpoints.

Generalized quadrilaterals of higher geometrical orders in (25) are used in SIE-MoM techniques [4], [43], [45], VSIE techniques [9], [79], and MoM-PO techniques [44], [46]. Their planar curvilinear version is used in 2-D FEM modeling [105]. Bilinear quadrilaterals in (27) are used with higher order current approximations in SIE techniques [2], [3], [38], [40]–[42] and VSIE techniques [41], [78].

B. Generalized Curved Parametric Triangles

Another attractive and effective geometrical modeling technique for arbitrary surfaces is based on using generalized curved parametric triangles as basic building blocks for mesh generation. A generalized triangle is commonly represented in terms of simplex coordinates (also referred to as normalized area coordinates), ξ_1, ξ_2, and ξ_3, as shown in Fig. 3. Namely, the parent domain is now an equilateral triangle with a unit height ($h = 1$), and edges equal to $a = 2/\sqrt{3}$. The coordinates ξ_1, ξ_2, and ξ_3 of an arbitrary point inside the triangle are defined as the normal distances of the point to the triangle edges across from vertices 1, 2, and 3, respectively. It is easily seen that the range of values for each of these parameters is from 0 to 1. It is also obvious that they are not independent from each other, as any two of them uniquely determine the position of the point. In addition, the lines connecting the point (ξ_1, ξ_2, ξ_3) to the triangle vertices break the triangle into three subtriangles with heights ξ_1, ξ_2, and ξ_3, and areas $\xi_1/\sqrt{3}$, $\xi_2/\sqrt{3}$, and $\xi_3/\sqrt{3}$, respectively. Since the sum of these subareas gives the area of the equilateral triangle, which, in turn, equals $1/\sqrt{3}$, we have

$$\xi_1+\xi_2+\xi_3 = 1. \qquad (29)$$

Mapping from the planar equilateral unit-height triangle in a local simplex coordinate system to a curved triangle in the global 3-D coordinate system (see Fig. 3), or vice versa, is defined by the parametric equation

$$\mathbf{r} = \mathbf{r}(\xi_1,\xi_2,\xi_3), \quad 0 \le \xi_1,\xi_2,\xi_3 \le 1. \qquad (30)$$

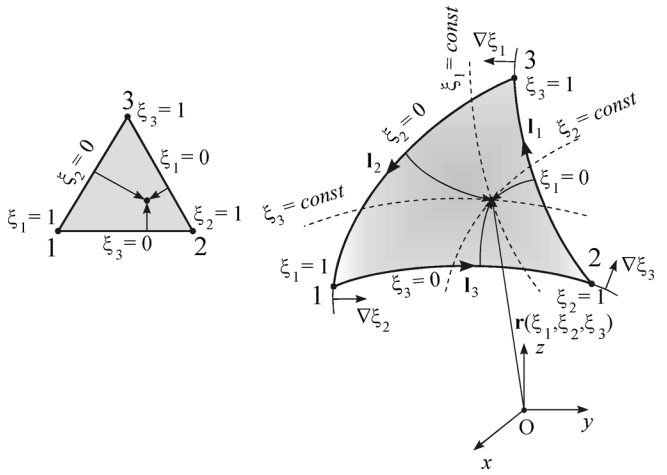

Fig. 3. Generalized curved parametric triangle defined by (30), with the parent domain in the form of an equilateral triangle of unit height.

Analogous higher order polynomial surface expansion to that in (24) for generalized quadrilaterals can be used for generalized triangles as well. Adopting the equidistant distribution of interpolation nodes along each simplex coordinate, the steps along ξ_1, ξ_2, and ξ_3 are given, respectively, by m/K, n/K, and p/K, with $m, n, p = 0, 1, 2, \ldots, K$, where K is the adopted geometrical order of the element (the same for all coordinates). From (29), $m+n+p=K$, and (30) becomes

$$\mathbf{r}(\xi_1,\xi_2,\xi_3) = \sum_{\substack{m,n,p=0 \\ (m+n+p=K)}}^{K} \mathbf{r}_{mnp} R_m^K(\xi_1) R_n^K(\xi_2) R_p^K(\xi_3). \tag{31}$$

Here, $\mathbf{r}_{mnp}$ are position vectors of interpolation nodes and R are Silvester–Lagrange interpolation polynomials of order K

$$R_m^K(\xi) = \begin{cases} \frac{1}{m!}\prod_{i=0}^{m-1}(K\xi - i), & 1 \le m \le K \\ 1, & m = 0 \end{cases}. \tag{32}$$

Note that R_m^K is unity at $\xi = m/K$ and zero at $\xi = 0, 1/K, 2/K, \ldots, (m-1)/K$.

Element of the lowest order, $K = 1$, is a flat triangle, with (31) yielding

$$\mathbf{r}(\xi_1,\xi_2,\xi_3) = \mathbf{r}_{100}\xi_1 + \mathbf{r}_{010}\xi_2 + \mathbf{r}_{001}\xi_3 \tag{33}$$

and $\mathbf{r}_{100}$, $\mathbf{r}_{010}$, and $\mathbf{r}_{001}$ being the position vectors of the triangle vertices. Fig. 4 shows the generalized Silvester–Lagrange triangle of the fourth geometrical order ($K = 4$), defined by $M = 15$ interpolation nodes with $m+n+p=4$.

Generalized triangles of higher geometrical orders in (31) are used in SIE techniques [4], [25], [49], [50], [52], [53], [58], SIE-Green's function techniques [51], [59], and FE-BI techniques [93]–[95], [97]. Their planar curvilinear version is used in 2-D FEM techniques [87], [100], [113], [118].

C. Generalized Curved Parametric Hexahedra

Volumetric modeling of arbitrary electromagnetic structures can be carried out using generalized curved parametric hexahedra defined by

$$\mathbf{r} = \mathbf{r}(u,v,w), \quad -1 \le u,v,w \le 1. \tag{34}$$

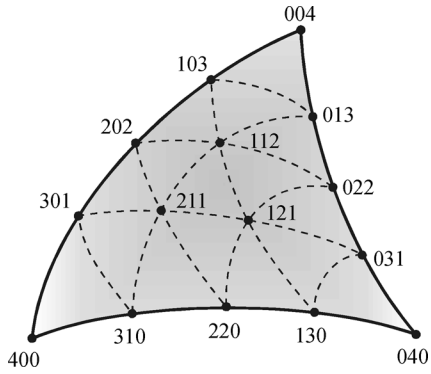

Fig. 4. Generalized Silvester–Lagrange triangle (31) of the fourth geometrical order ($m+n+p=4$) [24].

These elements represent a volume (3-D) generalization of quadrilateral patches in Fig. 1. Thus, the Lagrange-type interpolation hexahedron of arbitrary geometrical orders K_u, K_v, and K_w ($K_u, K_v, K_w \ge 1$), as the generalization of (25), is given by

$$\mathbf{r}(u,v,w) = \sum_{m=0}^{K_u}\sum_{n=0}^{K_v}\sum_{p=0}^{K_w} \mathbf{r}_{mnp} L_m^{K_u}(u) L_n^{K_v}(v) L_p^{K_w}(w). \tag{35}$$

Fig. 5(a) shows the first-order element ($K_u = K_v = K_w = 1$; $M = 8$ interpolation points–element vertices), called the trilinear hexahedron, whose faces are bilinear quadrilateral surfaces in Fig. 2(a). Its equation is

$$\begin{aligned}\mathbf{r}(u,v,w) &= \frac{1}{8}[\mathbf{r}_{000}(1-u)(1-v)(1-w) \\ &\quad + \mathbf{r}_{100}(u+1)(1-v)(1-w) \\ &\quad + \cdots + \mathbf{r}_{111}(u+1)(v+1)(w+1)] \\ &= \mathbf{b}_{000} + \mathbf{b}_{100}u + \mathbf{b}_{010}v + \mathbf{b}_{001}w \\ &\quad + \mathbf{b}_{110}uv + \mathbf{b}_{101}uw + \mathbf{b}_{011}vw + \mathbf{b}_{111}uvw. \end{aligned} \tag{36}$$

Also shown, in Fig. 5(b), is the triquadratic hexahedron ($K_u = K_v = K_w = 2$), determined by $M = 27$ interpolation points arbitrarily positioned in space.

Generalized hexahedra of higher geometrical orders in (35) are used in VIE techniques [74], [75], VSIE techniques [9], [79], FEM techniques [102]–[104], and FE-BI techniques [9], [85]. Trilinear hexahedra in (36) are used with higher order current approximations in VIE techniques [70]–[72] and VSIE modeling [41], [78].

D. Generalized Curved Parametric Tetrahedra

Extending the triangular curved surface in Fig. 3 to a volumetric element, a generalized curved parametric tetrahedron is obtained, described analytically by the following equation in simplex coordinates (normalized volume coordinates) ξ_1, ξ_2, ξ_3, and ξ_4:

$$\mathbf{r} = \mathbf{r}(\xi_1,\xi_2,\xi_3,\xi_4), \quad 0 \le \xi_1,\xi_2,\xi_3,\xi_4 \le 1, \quad \xi_1+\xi_2+\xi_3+\xi_4 = 1. \tag{37}$$

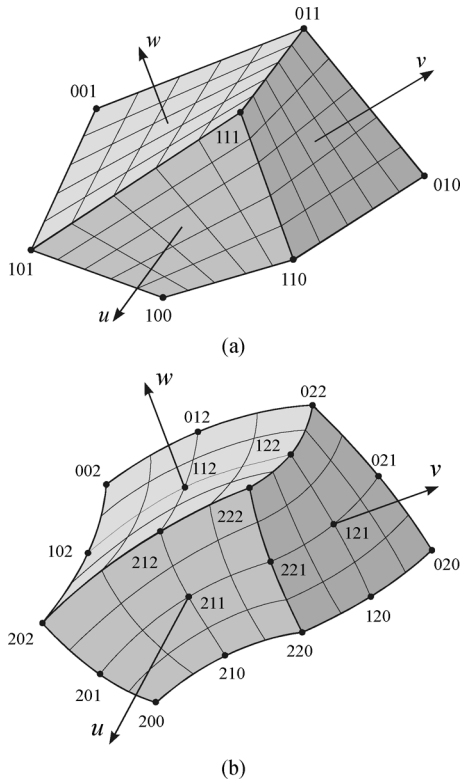

Fig. 5. Examples of Lagrange generalized hexahedra in (35): (a) trilinear hexahedron in (36) and (b) triquadratic hexahedron ($K_u = K_v = K_w = 2$).

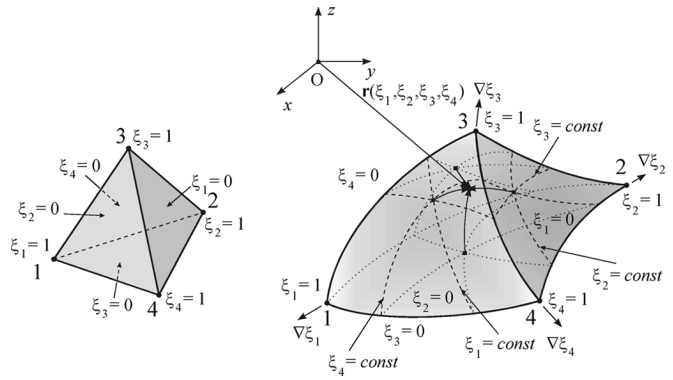

Fig. 6. Generalized curved parametric tetrahedron defined by (37), with parent unit-height equilateral tetrahedron.

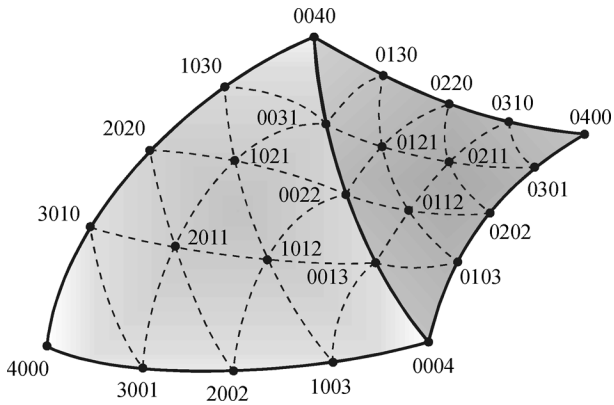

Fig. 7. Generalized Silvester–Lagrange tetrahedron (38) of the fourth geometrical order ($m + n + p + q = 4$) [24].

As indicated in Fig. 6, the coordinates of a point inside a parent equilateral tetrahedron of unit height in the local simplex coordinate system, which is mapped to a curvilinear tetrahedron in the global Cartesian coordinate system, represent the normal distances to the corresponding (flat) faces of the equilateral tetrahedron. The above relationship between the coordinates expresses the fact that the volumes of subtetrahedra defined by the point $(\xi_1, \xi_2, \xi_3, \xi_4)$ and any three of the vertices 1, 2, 3, and 4 in the local system add up to the volume of the equilateral tetrahedron. The volumetric version of (31) is a quadruple Silvester–Lagrange interpolation polynomial of order K in coordinates ξ_1, ξ_2, ξ_3, and ξ_4,

$$\mathbf{r}(\xi_1,\xi_2,\xi_3,\xi_4) = \sum_{\substack{m,n,p,q=0 \\ (m+n+p+q=K)}}^{K} \mathbf{r}_{mnpq} R_m^K(\xi_1) R_n^K(\xi_2) R_p^K(\xi_3) R_q^K(\xi_4). \quad (38)$$

For $K = 1$, we have a simple tetrahedron with all straight edges (and flat faces)

$$\mathbf{r}(\xi_1,\xi_2,\xi_3,\xi_4) = \mathbf{r}_{1000}\xi_1 + \mathbf{r}_{0100}\xi_2 + \mathbf{r}_{0010}\xi_3 + \mathbf{r}_{0001}\xi_4 \quad (39)$$

where $\mathbf{r}_{1000}$, $\mathbf{r}_{0100}$, $\mathbf{r}_{0010}$, and $\mathbf{r}_{0001}$ are the position vectors of its vertices. As a higher order example, shown in Fig. 7 is a curved tetrahedron with $K = 4$ $(m + n + p + q = 4)$.

Generalized tetrahedra of higher geometrical orders in (38) are used for FEM modeling in [25], [88], [93]–[95], and [97].

Note that, in general, CEM models with tetrahedra and triangles require considerably more unknowns than the corresponding models with hexahedra and quadrilaterals.

IV. Higher Order Current and Field Modeling

A. Higher Order Hierarchical Divergence-Conforming Basis Functions on Generalized Quadrilaterals

The first class of basis functions on generalized quadrilaterals (Fig. 1) is a set of divergence-conforming hierarchical-type vector basis functions representing a higher order generalization of rooftop functions [134] constructed from simple power functions (P) in parametric coordinates u and v. With them, the electric surface current density vector over generalized quadrilaterals (in the MoM-SIE model) is approximated as

$$\mathbf{J}_{\mathrm{s}} = \frac{1}{\Im}\left[\sum_{\mathrm{i}=0}^{N_u}\sum_{j=0}^{N_v-1} \alpha_{ij}^{(u)} f_{ij}^{(u)}(u,v)\mathbf{a}_u + \sum_{\mathrm{i}=0}^{N_u-1}\sum_{j=0}^{N_v} \alpha_{ij}^{(v)} f_{ij}^{(v)}(u,v)\mathbf{a}_v\right]$$
$$f_{ij}^{(u)} = \hat{P}_{\mathrm{i}}(u)P_j(v), \quad f_{ij}^{(v)} = P_{\mathrm{i}}(u)\hat{P}_j(v) \quad (40)$$

where $\hat{P}$ denotes modified (divergence-conforming) power functions

$$\hat{P}_{\rm i}(u)=\begin{cases}1-u, & i=0\\ u+1, & i=1\\ u^i-1, & i\geq 2,\ \text{even}\\ u^i-u, & i\geq 3,\ \text{odd}\end{cases}$$
$$P_j(v)=v^j, \quad -1\leq u,v\leq 1. \quad (41)$$

N_u and N_v ($N_u, N_v \geq 1$) are the adopted degrees of the polynomial current approximation in the u- and v-direction, respectively, which are entirely independent from the element geometrical orders (K_u and K_v), $\{\alpha\}$ are unknown current-distribution coefficients, and $\Im$ is the Jacobian of the covariant transformation, found from the unitary vectors $\mathbf{a}_u$ and $\mathbf{a}_v$ along the parametric coordinates

$$\Im=|\mathbf{a}_u\times\mathbf{a}_v|, \quad \mathbf{a}_u=\frac{\partial\mathbf{r}}{\partial u}, \quad \mathbf{a}_v=\frac{\partial\mathbf{r}}{\partial v} \qquad (42)$$

with $\mathbf{r}$ given in (23). Note that the lowest order of approximation ($N_u=N_v=1$) yields the rooftop functions on generalized quadrilateral patches. For any j ($0\leq j\leq N_v-1$), the basis functions $(1-u)v^j$ (for $i=0$) and $(u+1)v^j$ (for $i=1$) serve for adjusting the continuity condition for the normal component of $\mathbf{J}_{\rm s}$ along edges $u=-1$ and $u=1$, respectively, of the element (divergence conformity), while the remaining basis functions (for $2\leq i\leq N_u$) are zero at the quadrilateral edges and serve for improving the current approximation over the surface. From (40)–(42), this vector component for the edge $u=-1$, for instance, is

$$(J_{\rm s})_{\rm norm}=J_{su}\sin\theta_{uv}=J_{su}(-1,v)\,\frac{|\mathbf{a}_u\times\mathbf{a}_v|}{|\mathbf{a}_u||\mathbf{a}_v|}$$
$$=\frac{2}{|\mathbf{a}_v(-1,v)|}\sum_{j=0}^{N_v-1}\alpha_{0j}^{(u)}v^j \quad (\text{at edge } u=-1) \qquad (43)$$

where J_{su} denotes the u-component of $\mathbf{J}_{\rm s}$ at the edge (the v-component of $\mathbf{J}_{\rm s}$ is tangential to the edge), and θ_{uv} the angle between the u and v parametric lines at the same point. Since the unitary vector along the edge, $\mathbf{a}_v(-1,v)$, is the same for the two adjacent elements sharing the edge, the continuity condition between the elements, for $-1\leq v\leq 1$, can readily (automatically) be enforced, regardless of the adopted geometrical orders, current-expansion orders, or local orientations of the elements. The only requirement that needs to be satisfied is the geometrical compatibility of the joint edge. The current continuity is imposed by equating the corresponding normal-vector coefficients, $\alpha_{0j}^{(u)}$ in (43), associated with the elements, so that these coefficients are common for the two elements, with additional corrections (sign change) due to possibly different element orientations. For elements with different geometrical orders along the common edge, K_v in (25), the same parametric presentations on both sides of the junction are ensured by placing the interpolation nodes of the element with a higher order at positions that match the parameter values already determined by the interpolation nodes of the element with a lower order. For elements with different current-expansion orders along the junction, N_v-1 in (43), the normal-vector coefficients are matched only up to the lesser of the two orders and are set to zero for the remaining normal-vector basis functions. This order reduction pertains to the common edge only and does not influence the expansions over the rest of the surfaces of the elements. More general discussions of different types of surface-element junctions and procedures of adjusting the higher order bases to ensure divergence conformity at boundaries between curved elements are provided in [3] and [4], respectively.

Using high orders N_u and N_v enables using large curved MoM quadrilaterals that are on the order of λ (e.g., $1\lambda-2\lambda$) in each dimension as building blocks for modeling of the electromagnetic structure (i.e., the boundary elements can be by two orders of magnitude larger in area than traditional low-order boundary elements). Note that the sum limits in (40) that correspond to the variations of a current density vector component in the direction across that component are by one smaller than the orders corresponding to the variations in the other parametric coordinate. This mixed-order arrangement, which ensures equal approximation orders for surface charge densities corresponding to the u- and v-directed current basis functions, has been found to be a preferable choice for modeling of surface currents in all applications. Basis functions in (40) and (41) are used for modeling of both electric and magnetic surface currents, $\mathbf{J}_{\rm s}$ and $\mathbf{M}_{\rm s}$, on generalized quadrilaterals of higher geometrical orders (25) in the SIE technique for arbitrary material structures [43]. They are used in conjunction with bilinear quadrilaterals (27) in the SIE technique for PEC structures [2], SIE techniques for arbitrary material structures [3], [40], [41], and VSIE technique based on (10) [41], [78].

Hierarchical higher order basis functions, in general, enable using different orders of current/field approximation in different (surface or volume) elements in the model for efficient selective discretization of the solution domain, because each lower-order set of functions is a subset of higher order sets. For instance, the hierarchical nature of basis functions in (40)–(41) and selective adoption of orders N_u and N_v in different quadrilaterals allow for a whole spectrum of quadrilateral sizes (e.g., from a very small fraction of λ to a couple of λ) and the corresponding current approximation orders to be used at the same time in a single simulation model of a complex structure. Additionally, each individual element can have drastically different edge lengths, enabling a whole range of "regular" and "irregular" quadrilateral shapes (e.g., square-shaped, rectangular, strip-like, trapezoidal, triangle-like, etc.) to be used in a simulation model as well. Hierarchical basis functions, on the other hand, generally have poor orthogonality properties, which results in MoM/FEM matrices with large condition numbers. This affects the overall accuracy and stability of the solution. Most importantly, if the matrix equation associated with the MoM/FEM is solved using iterative solvers, the overall computation time is much larger when the corresponding matrices are badly conditioned (e.g., the number of iterations for conjugate gradient solvers is proportional to the square root of the condition number).

Orthogonality and conditioning properties of hierarchical higher order basis functions in (40) can be significantly improved, and made comparable to those of interpolatory bases,

if basis functions f_{ij}, other than rooftop functions, are constructed from standard orthogonal polynomials instead of power expansions. A notable example is the following class of Legendre basis functions [45]:

$$\hat{P}_{\mathrm{i}}(u)=\hat{C}_{\mathrm{i}}\left\{\begin{array}{cc}1-u, & i=0\\ u+1, & i=1\\ Q_{\mathrm{i}}(u)-Q_{\mathrm{i}-2}(u), & i\geq 2\end{array}\right\},\ P_j(v)=C_jQ_j(v)$$

$$Q_{\mathrm{i}}(u)=\frac{1}{2^i i!}\frac{\mathrm{d}^i}{\mathrm{d}u^i}(u^2-1)^i,\quad -1\leq u,v\leq 1 \tag{44}$$

where Legendre polynomials Q [135] defined on the interval $[-1, 1]$, which have nonzero values at the interval boundaries, are combined to form polynomials $\hat{P}$ for $i \geq 2$ in a divergence-conforming fashion. Namely, using the difference of the polynomials Q of orders i and $i-2$ as the basis function of order i in approximating the variation of the u-component of the current density vector $\mathbf{J}_{\mathrm{s}}$ in (40) along the u coordinate, and analogously for the v-component of $\mathbf{J}_{\mathrm{s}}$, makes the higher order expansions for the normal component of $\mathbf{J}_{\mathrm{s}}$ zero across edges shared by adjacent generalized quadrilaterals and allows for the maximum number of basis functions to be mutually orthogonal within the solution procedure. The scaling factors C and $\hat{C}$ are adopted to further reduce the condition number by ensuring that the Euclidean norm of basis functions is unity on a square patch of unit side length [45]. Similar classes of higher order hierarchical MoM basis functions with improved conditioning constructed from other types of standard orthogonal polynomials, e.g., Chebyshev polynomials, are also used [42].

B. Higher Order Interpolatory Divergence-Conforming Basis Functions on Generalized Triangles

The next class of higher order basis functions are divergence-conforming interpolatory vector basis functions (for modeling of surface currents) on generalized triangles (in Fig. 3). Here, we start with Rao–Wilton–Glisson (RWG) basis functions [136], which are a simplex counterpart of rooftop functions on quadrilateral patches. The RWG function associated with edge 1 of the triangle in Fig. 3 (edge across vertex 1) can be expressed in simplex coordinates as

$$\mathbf{\Lambda}_1(\xi_1,\xi_2,\xi_3)=\frac{1}{\Im}(\xi_2\mathbf{l}_3-\xi_3\mathbf{l}_2) \tag{45}$$

and analogous expressions hold for the functions for the other two edges. The Jacobian and unitary vectors are obtained as

$$\Im=\mathbf{a}_1\cdot(\mathbf{a}_2\times\mathbf{a}_3),\quad \mathbf{a}_m=\frac{\partial\mathbf{r}}{\partial\xi_m}\quad (m=1,2,3) \tag{46}$$

where $\mathbf{r}$ is given in (30), and the edge vectors $\mathbf{l}_m$ $(m=1,2,3)$ in Fig. 3 as

$$\mathbf{l}_1=-\mathbf{a}_2,\quad \mathbf{l}_2=\mathbf{a}_1,\quad \mathbf{l}_3=\mathbf{a}_2-\mathbf{a}_1. \tag{47}$$

The function $\mathbf{\Lambda}_1$ has a normal component only on edge 1, which, moreover, is constant along the edge, so that the current continuity can be automatically adjusted with the accompanying RWG function on the adjacent patch across the edge. The higher order basis functions are generated by multiplying the RWG functions by combinations of Silvester–Lagrange interpolation polynomials (32), where the same mesh of interpolation nodes is used for interpolating the current distribution as for the geometrical transformation in Fig. 3. However, not all nodes in the mesh are used for individual basis functions. Namely, the interpolation polynomials multiplying the function $\mathbf{\Lambda}_1$ are defined on a subset of interpolation nodes that does not include those residing on edges 2 and 3, along which the normal components of $\mathbf{\Lambda}_1$ vanish, and analogously for polynomials multiplying RWG functions $\mathbf{\Lambda}_2$ and $\mathbf{\Lambda}_3$. Therefore, the order of the current approximation, i.e., the order to which the basis functions are complete, on the element (the same in all three simplex directions), N, is, in effect, by two smaller than the geometrical (mapping) order of the element, K, as illustrated in Fig. 8. With this, the basis function of order N for edge 1 corresponding to the interpolation node (i,j,k) is given by [25], [24]

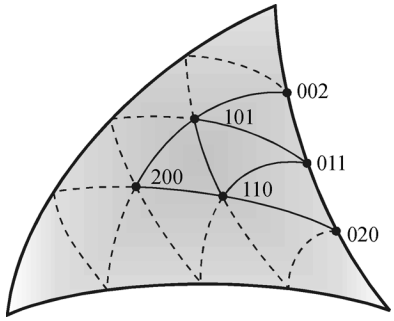

Fig. 8. A subset of interpolation nodes used in (48) for $N=2$, for basis functions associated with edge 1 of the triangle, obtained by shifting the nodes in Fig. 4 away from edges 2 and 3 [24].

$$\begin{aligned}&\mathbf{\Lambda}^{(1)}_{ijk}(\xi_1,\xi_2,\xi_3)\\ &\quad=C^{(1)}_{ijk}R^{N+2}_{\mathrm{i}}(\xi_1)\hat{R}^{N+2}_j(\xi_2)\hat{R}^{N+2}_k(\xi_3)\mathbf{\Lambda}_1(\xi_1,\xi_2,\xi_3)\\ &\quad 0\leq\xi_1,\xi_2,\xi_3\leq 1,\quad i=0,1,\ldots,N\\ &\quad j,k=1,2,\ldots,N+1,\ \ i+j+k=N+2=K\end{aligned} \tag{48}$$

where $C^{(1)}_{ijk}$ is the normalization factor chosen to make the normal component of $\mathbf{\Lambda}^{(1)}_{ijk}$ unity along edge 1, and $\hat{R}$ are shifted Silvester–Lagrange interpolation polynomials, defined as

$$\hat{R}^K_m(\xi)=\left\{\begin{array}{ll}\frac{1}{(m-1)!}\prod_{i=1}^{m-1}(K\xi-i), & 2\leq m\leq K+1\\ 1, & m=1\end{array}\right. . \tag{49}$$

The shifted polynomials enable shifting of the array of the interpolation nodes away from edges 2 and 3, toward the interior of the triangle, as in Fig. 8 (note that $\hat{R}^K_m$ does not have a zero at $\xi=0$). Analogous expansions are used for basis functions $\mathbf{\Lambda}^{(2)}_{ijk}$ and $\mathbf{\Lambda}^{(3)}_{ijk}$. By visualizing the node arrays for $\mathbf{\Lambda}^{(2)}_{ijk}$ and $\mathbf{\Lambda}^{(3)}_{ijk}$ corresponding to that for $\mathbf{\Lambda}^{(1)}_{ijk}$ in Fig. 8, we realize that the nodes in the interior of the triangle appear in the interpolation pattern three times, i.e., three different vector basis functions, $\mathbf{\Lambda}^{(1)}_{ijk}$, $\mathbf{\Lambda}^{(2)}_{ijk}$, and $\mathbf{\Lambda}^{(3)}_{ijk}$, interpolate the unknown surface vector function ($\mathbf{J}_{\mathrm{s}}$) at each of the interior nodes. However,

a 2-D vector function has only two degrees of freedom, which implies that the three basis functions are linearly dependent, so one of them must be eliminated from the set to obtain a unique solution. Note that, combining (45)–(48) and (29), the surface expansion for $\mathbf{J}_{\rm s}$ on a generalized triangle can be written as

$$\mathbf{J}_{\rm s} = \frac{1}{\Im}\left[J_1(\xi_1,\xi_2)\mathbf{a}_1 + J_2(\xi_1,\xi_2)\mathbf{a}_2\right] \tag{50}$$

which resembles that in (40) for a generalized quadrilateral. As the total number of interior nodes is $N(N+1)/2$, the number of unknowns in the interior is $N(N+1)$. On the other side, the nodes along edges appear only once in the interpolation pattern, resulting in only one vector basis function for each edge node, except for the nodes at triangle vertices, which are not included at all. Hence, the number of edge unknowns is $3(N+1)$, for a total of $(N+1)(N+3)$ unknowns per triangle. Of course, edge unknowns that are common for the patches sharing the edge should be counted only once, which effectively reduces the overall number of unknowns in the model.

Basis functions in (48), on higher order generalized triangles, are used in SIE techniques for modeling of PEC structures in free space [4], [25], [49], [50], [58], and in layered media [51]. They are also used in SIE models involving arbitrary material structures [52], as well as for FE-BI modeling [93]–[95].

Interpolatory higher order basis functions, in general, have excellent orthogonality properties and produce well-conditioned MoM/FEM matrices. In addition, there is a direct physical interpretation of every current- or field-distribution coefficient in the model, since only one basis function is nonzero at every interpolation point. However, in divergence- or curl-conforming arrangements, interpolatory bases require that the orders of current/field approximation must be kept constant throughout the model, implying that all elements in the model must be about the same size. For instance, the (high) order N for basis functions in (48) must be the same for all generalized triangular patches in the SIE mesh, which, accordingly, should be approximately equally sized and nearly equilateral (N is the same for all three edges in a triangle). This considerably limits the modeling flexibility of interpolatory higher order techniques.

C. Higher Order Spatial/Temporal Basis Functions for TDIE Modeling

In higher order TDIE techniques, a higher order spatial discretization of currents is combined with a temporal discretization based on the marching-on-in-time (MOT) scheme [53]. For an SIE formulation of transient scattering from PEC surfaces, the surface currents can be approximated as [53]

$$\mathbf{J}_{\rm s}(\mathbf{r},t) = \sum_{i=1}^{N_{\rm t}}\sum_{j=1}^{N_{\rm s}} \alpha_{ij} T(t-i\Delta t)\mathbf{\Lambda}_{(j)}(\mathbf{r}) \tag{51}$$

where T are scalar temporal basis functions and $\mathbf{\Lambda}$ are vector spatial basis functions adopted in the form of higher order divergence-conforming interpolatory polynomials (48) on generalized triangles, and $N_{\rm t}$ and $N_{\rm s}$ are their respective total numbers in the model. The time steps are $\Delta t = \pi/(s\omega_0)$, with ω_0 being the maximum angular frequency of the incident field (the field is assumed to be temporally bandlimited to ω_0) and $s > 1$ an oversampling factor (typically on the order of 10). In [53], T are chosen to be bandlimited interpolatory functions (BLIFs) defined as the product of an approximate prolate spheroidal wave function (APSWF) and sinc function

$$T(t) = \frac{\sin(s\omega_0 t)}{s\omega_0 t}\frac{\sin\left[a\sqrt{\left(\frac{t}{N_w\Delta t}\right)^2-1}\right]}{\sinh(a)\sqrt{\left(\frac{t}{N_w\Delta t}\right)^2-1}} \tag{52}$$

where N_w is the APSWF width parameter and $a = \pi N_w(s-1)/s$ is the time-bandwidth product of the APSWF. However, the BLIFs cannot be directly implemented into the MOT scheme as this would result in a noncausal system, and hence an extrapolation technique, based on the linear least square approach, is used to recover time marching with BLIFs by extrapolating (predicting) future current samples from the values of past currents.

D. Higher Order Point-Based Basis Functions on Generalized Quadrilaterals and Triangles

In point-based SIE techniques, such as those based on the Nyström discretization [137], [28], the unknown surface currents are represented by their samples at a set of discrete points on the surface geometrical elements (patches) in the model. These techniques do not automatically stipulate the current continuity across junctions between patches and do not enforce divergence-conformity of basis functions, allowing the use of defective meshes, where element edges in junctions are not necessarily entirely shared by the two adjacent patches. Hence, a nonconforming form of higher order Legendre basis functions on generalized quadrilateral patches, as simple products of Legendre polynomials [see (44)]

$$f_{ij}^{(u)} = f_{ij}^{(v)} = Q_{\rm i}(u)Q_j(v), \quad -1 \le u,v \le 1 \tag{53}$$

in the vector expansion for $\mathbf{J}_{\rm s}$ in (40), can be used for a point-based (Nyström) discretization, with the SIE sampled at the quadrature points defined by the two-fold Gauss–Legendre integration formula [55].

On the other side, point-based discretizations on generalized triangular patches [58] employ products of Silvester–Lagrange interpolation polynomials, (32), in simplex coordinates in Fig. 3

$$f_{ijk} = R_{\rm i}^N(\xi_1)R_j^N(\xi_2)R_k^N(\xi_3), \quad 0 \le \xi_1,\xi_2,\xi_3 \le 1, \quad i+j+k = N \tag{54}$$

for each component of $\mathbf{J}_{\rm s}$, where N is the order of the interpolation. Interpolation nodes (i,j,k) are chosen to be the same as the integration points of Gauss–Legendre quadratures.

E. Higher Order Curl-Conforming Basis Functions on Generalized Quadrilaterals and Triangles

The curl-conforming version of hierarchical higher order basis functions on generalized quadrilaterals in (40)–(42), used,

for instance, in 2-D FEM computation of the transversal electric field intensity vector ($\mathbf{E}$) in the cross section of arbitrary electromagnetic waveguides [105], is given by

$$\begin{aligned}\mathbf{E} = &\sum_{i=0}^{N_u-1}\sum_{j=0}^{N_v}\alpha_{ij}^{(u)}P_{\mathrm{i}}(u)\hat{P}_j(v)\mathbf{a'}_u \\ &+\sum_{i=0}^{N_u}\sum_{j=0}^{N_v-1}\alpha_{ij}^{(v)}\hat{P}_{\mathrm{i}}(u)P_j(v)\mathbf{a'}_v \\ &-1\le u,v\le 1. \end{aligned} \tag{55}$$

Here, $\mathbf{a}'_u$ and $\mathbf{a}'_v$ are the reciprocal unitary vectors, obtained as

$$\mathbf{a}'_u = \frac{\mathbf{a}_v\times\mathbf{n}}{\Im}, \quad \mathbf{a}'_v = \frac{\mathbf{n}\times\mathbf{a}_u}{\Im} \tag{56}$$

with $\mathbf{n}$ denoting the unit vector normal to the surface of the element. Rooftop functions $1\mp v$ (for $j=0,1$) in the reciprocal E_u field component in (55) are coupled across the edges $v=\mp 1$ with the corresponding rooftops in adjacent elements in the tangential-field continuity boundary conditions (curl conformity), and similarly for the E_v component at the edges $u=\mp 1$ [with analogous expressions for E_{tang} as in (43)]. We note that, just opposite to the divergence-conforming expansion in (40), the reciprocal u-component of the vector is associated, in terms of the conformity requirement, with $v=\mp 1$ edges, and vice versa. We also note that the vector basis function counterparts in (40) and (55), a u-directed divergence-conforming and v-reciprocal curl-conforming function and vice versa (including the adjustment of the sign for the right-handedness of the u-v coordinate system with respect to the normal $\mathbf{n}$), are related as

$$\mathbf{f}_{\text{curl-conforming}} = \mathbf{n}\times\mathbf{f}_{\text{div-conforming}}. \tag{57}$$

We note finally a reciprocal, with respect to (40), mixed-order arrangement of sum limits in (55).

For generalized triangles (Fig. 3), the simplex coordinate gradients are $\nabla\xi_m = \mathbf{n}\times\mathbf{l}_m/\Im$ $(m=1,2,3)$ [25], so (57) gives the following expression for the curl-conforming version of the zeroth-order (RWG) bases in (45):

$$\begin{aligned}\mathbf{\Omega}_1(\xi_1,\xi_2,\xi_3) = \mathbf{n}\times\mathbf{\Lambda}_1 = \xi_2\nabla\xi_3 - \xi_3\nabla\xi_2, \\ 0\le\xi_1,\xi_2,\xi_3\le 1\end{aligned} \tag{58}$$

which are known as Whitney forms. The higher order curl-conforming interpolatory basis functions associated with edge 1 of the triangle in Fig. 3 (and Fig. 8), $\mathbf{\Omega}_{ijk}^{(1)}$, are then obtained by merely replacing $\mathbf{\Lambda}_1$ by $\mathbf{\Omega}_1$ in (48), and analogously for $\mathbf{\Omega}_{ijk}^{(2)}$ and $\mathbf{\Omega}_{ijk}^{(3)}$. These bases are used in 2-D FEM modeling [100].

Note that higher order sets of divergence- and curl-conforming interpolatory basis functions defined on generalized curved quadrilaterals, analogous to those on triangles, are also available [25], [4]. On the other side, very effective sets of hierarchical higher order basis functions for triangular elements, suitable for p-adaption, are developed in both divergence-conforming [37], [4] and curl-conforming [91], [4] arrangements.

F. Higher Order Hierarchical Divergence- and Curl-Conforming Bases on Generalized Hexahedra

For VIE and VSIE hierarchical modeling using generalized hexahedral elements in (34) and Fig. 5, a 3-D generalization of divergence-conforming higher order 2-D vector bases in (40) is used for the approximation of the electric flux density vector [see (9)], $\mathbf{D}=\mathbf{D}_u+\mathbf{D}_v+\mathbf{D}_w$, in parametric coordinates u, v, and w,

$$\begin{aligned}\mathbf{D}_u = &\frac{1}{\Im}\sum_{i=0}^{N_u}\sum_{j=0}^{N_v-1}\sum_{k=0}^{N_w-1}\alpha_{ijk}^{(u)}\hat{P}_{\mathrm{i}}(u)P_j(v)P_k(w)\mathbf{a}_u \\ &\Im = (\mathbf{a}_u\times\mathbf{a}_v)\cdot\mathbf{a}_w, \quad -1\le u,v,w\le 1\end{aligned} \tag{59}$$

with analogous expressions for vector components $\mathbf{D}_v$ and $\mathbf{D}_w$, where P and $\hat{P}$ are power expansions in (41) [41], [70]–[72], [78] or Legendre expansions in (44) [75]. These bases ensure continuity of the normal component of $\mathbf{D}$ across sides shared by adjacent hexahedra in the model.

Curl-conforming hierarchical vector expansions for FEM computation on generalized hexahedra are now obtained as either a 3-D generalization of 2-D curl-conforming bases in (55) or a curl-conforming version of divergence-conforming 3-D bases in (59)

$$\begin{aligned}\mathbf{E}_u = &\sum_{i=0}^{N_u-1}\sum_{j=0}^{N_v}\sum_{k=0}^{N_w}\alpha_{ijk}^{(u)}P_{\mathrm{i}}(u)\hat{P}_j(v)\hat{P}_k(w)\mathbf{a'}_u, \\ &\mathbf{a}'_u = \frac{\mathbf{a}_v\times\mathbf{a}_w}{\Im}, \qquad -1\le u,v,w\le 1\end{aligned} \tag{60}$$

with analogous representations for the other two reciprocal components of $\mathbf{E}$, and versions combining power functions [102], [104] and Legendre polynomials [103]. The continuity of tangential fields over junctions of hexahedra is enforced.

G. Higher Order Interpolatory Curl-Conforming Basis Functions on Generalized Tetrahedra

FEM models based on higher order interpolatory tetrahedral elements (Fig. 6) [25], [88], [93]–[95] use a 3-D curl-conforming version of bases in (48). Labeling by m the face across vertex m $(m=1,2,3,4)$ of a tetrahedron, the 3-D zeroth-order curl-conforming basis (Whitney form) associated with the edge shared by faces 1 and 2 (i.e., the edge between vertices 3 and 4) is, from (58) for the 2-D one, given by

$$\mathbf{\Omega}_{12}(\xi_1,\xi_2,\xi_3,\xi_4) = \xi_4\nabla\xi_3 - \xi_3\nabla\xi_4 \tag{61}$$

and analogously for the remaining five edges of the tetrahedron. The function $\mathbf{\Omega}_{12}$ has tangential components only on faces 1 and 2, which are continuous across the boundary into adjacent elements (curl-conformity). Following (48), the resulting basis function of order N corresponding to the interpolation node (i,j,k,l) is then [25], [24]

$$\begin{aligned}&\mathbf{\Omega}_{ijkl}^{(12)}(\xi_1,\xi_2,\xi_3,\xi_4) \\ &= C_{ijkl}^{(12)}R_i^{N+2}(\xi_1)R_j^{N+2}(\xi_2)\hat{R}_k^{N+2}(\xi_3) \\ &\quad\cdot\hat{R}_l^{N+2}(\xi_4)\mathbf{\Omega}_{12}(\xi_1,\xi_2,\xi_3,\xi_4) \\ &0\le\xi_1,\xi_2,\xi_3,\xi_4\le 1,\ \ i,j=0,1,\ldots,N,\ \ k,l=1,2,\ldots,N+1 \\ &\quad i+j+k+l = N+2 = K\end{aligned} \tag{62}$$

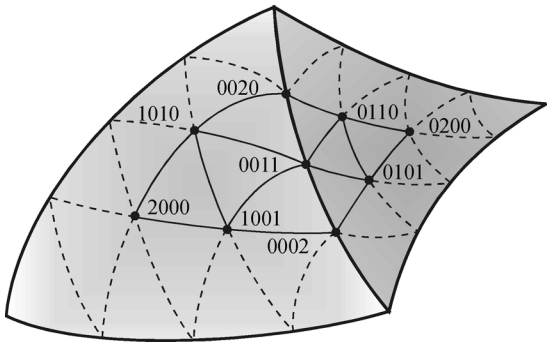

Fig. 9. Shifting of interpolation nodes in Fig. 7 away from faces 3 and 4 of the tetrahedron to form a subset of nodes used in (62) for $N = 2$, for bases associated with the edge shared by faces 1 and 2.

and analogous expressions, with permutations of indices, can be written for higher order bases associated with other edges. The same shifting of interpolation nodes actually used in (62), away from the faces over which the tangential components of $\mathbf{\Omega}_{12}$ vanish (faces 3 and 4 for this function), as in Fig. 8 in the 2-D case, applies here as well, which is illustrated in Fig. 9.

As for 2-D interpolations in (48), many of the basis functions provided by (62) have to be discarded as linearly dependent with other functions for the same interpolation node. In fact, the elimination rule for nodes at tetrahedron faces is exactly the same as for the triangular element and (48) – one basis function per node has to be eliminated, since tangential components of $\mathbf{E}$ have only two degrees of freedom. In addition, (62) provides six basis functions for an interior interpolation node (as there are a total of six edges), so three of them have to be discarded ($\mathbf{E}$ has three degrees of freedom throughout the volume of the element). With a similar calculation to that in the 2-D case, this results in a total of $(N+1)(N+3)(N+4)/2$ unknowns per tetrahedron.

Note that a hierarchical counterpart of bases in (62) for higher order tetrahedral finite elements is also available [91].

H. Higher Order Spatial/Temporal Field Expansions for TD-FEM Modeling

In higher order TD-FEM formulations, such as the one in (22), the spatially and temporally varying electric field can be approximated using higher order curl-conforming interpolatory spatial bases $\mathbf{\Omega}$ in (62), defined on generalized curved tetrahedral elements, with time-dependent field-distribution coefficients [97]

$$\mathbf{E}(\mathbf{r},t)=\sum_{i=1}^{N_\mathrm{s}}\alpha_i(t)\mathbf{\Omega}_i(\mathbf{r}) \tag{63}$$

where N_s denotes the total number of spatial functions in the model. The coefficients $\{\alpha\}$ are determined from the following set of second-order ordinary differential equations in time [97]:

$$[T]\frac{\mathrm{d}^2\{\alpha\}}{\mathrm{d}t^2}+([R]+[Q])\frac{\mathrm{d}\{\alpha\}}{\mathrm{d}t}+[S]\{\alpha\}+\{w\}=\{0\} \tag{64}$$

where the elements of matrices $[T]$, [R], and $[S]$ are the corresponding volume integrals, and $[Q]$ and $\{w\}$ surface integrals, with bases $\mathbf{\Omega}$ in integrands, e.g., integrals over V and S in (22) with $\mathbf{E}$ substituted by the appropriately indexed functions $\mathbf{\Omega}$. In [97], (64) is discretized in time by a standard central-difference scheme, and is solved in a time marching fashion.

I. Higher Order Singular Bases Incorporating Edge Effects

Finally, if the structure under consideration possesses sharp edges, the accuracy and efficiency of higher order current and field expansions near these edges can be improved by explicitly incorporating in basis functions the terms that exactly model the singular edge behavior of currents/fields. For instance, it is known that the component of the electric surface current density vector, $\mathbf{J}_\mathrm{s}$, parallel to the edge of a PEC wedge defined by an angle ϕ is proportional to ρ^{b-1}, ρ being the normal distance of the current element (on the wedge) from the edge and $b=\pi/(2\pi-\phi)$ the quasistatic singularity coefficient (note that $b=1/2$ for $\phi=0$, i.e., for a free edge of a plate – so-called knife edge) [138]. Therefore, modifying a given existing set of higher order basis functions for the approximation of $\mathbf{J}_\mathrm{s}$ such that this edge condition is satisfied, higher order singular bases are formed that provide higher order convergence of results near edges in a general PEC model.

Taking the set of higher order hierarchical divergence-conforming basis functions on generalized quadrilaterals in (40)–(41) as an example, the singular quasistatic effects associated with the edge $u=-1$ of the quadrilateral element in a PEC model are taken into account by multiplying the v-directed regular (nonsingular) basis functions $f_{ij}^{(v)}$ in (40) by the edge term for $u=-1$ [3], [39]

$$\left[f_{ij}^{(v)}\right]_{\text{singular}}=(1+u)^{b-1}f_{ij}^{(v)}\quad(\text{edge singularity at } u=-1) \tag{65}$$

and analogously for other edges of the element. Of course, for $b=1$, that is, $\phi=\pi$ (no edge), the singular functions reduce to regular ones.

As another example, for higher order interpolatory divergence-conforming bases on generalized triangles in (48), a similar transformation for the singularity at the edge 1 (for $\xi_1=0$) in the triangle in Fig. 3 gives the following singular version of functions $\mathbf{\Lambda}_{ijk}^{(2)}$ and $\mathbf{\Lambda}_{ijk}^{(3)}$ (that are tangential to this edge) [101]:

$$\left[\mathbf{\Lambda}_{ijk}^{(2)}\right]_{\text{singular}}=\xi_1{}^{b-1}\mathbf{\Lambda}_{ijk}^{(2)},\quad\left[\mathbf{\Lambda}_{ijk}^{(3)}\right]_{\text{singular}}=\xi_1{}^{b-1}\mathbf{\Lambda}_{ijk}^{(3)}\quad(\text{edge singularity at } \xi_1=0) \tag{66}$$

with analogous expressions for singularities at edges 2 and 3 of the triangle. In [101], this concept is expanded to also include the singular behavior of the normal component of $\mathbf{J}_\mathrm{s}$ and the associated surface charge density near the sharp edge. In fact, [101] provides complete sets of singular higher order interpolatory vector bases that incorporate the edge conditions on both generalized triangles and quadrilaterals in both divergence-conforming and curl-conforming formats. It as well provides a comprehensive survey of techniques for treating edge singularities in CEM, some being of higher order nature (e.g., an extension of higher order scalar hierarchical triangular basis functions for 2-D FEM analysis to better cope with edge singularities in waveguide problems [110]).

V. Higher Order Solution Techniques

A. Higher Order Galerkin Testing Procedures

In higher order CEM, both IEs (in MoM) and DEs (in FEM) are most frequently tested by means of the Galerkin method, i.e., using the same higher order functions used for current or field expansion. Taking the general SIE formulation in (6) and (7) as an example, the electric/electric and electric/magnetic generalized Galerkin impedances (the system matrix elements) corresponding to the electric-current testing functions $\mathbf{J}_{\mathrm{s}m}$ defined on the mth surface element (S_m) and the electric- and magnetic-current basis functions $\mathbf{J}_{\mathrm{s}n}$ and $\mathbf{M}_{\mathrm{s}n}$ defined on the nth element in the model, for one of the material domains, are given by [43]

$$\begin{aligned} Z_{mn}^{\mathrm{ee}} &= \eta \int_{S_m} \mathbf{J}_{\mathrm{s}m} \cdot \mathbf{L}(\mathbf{J}_{\mathrm{s}n}) \mathrm{d}S_m \\ &= \mathrm{j}\omega\mu \int_{S_m} \int_{S_n} \mathbf{J}_{\mathrm{s}m} \cdot \mathbf{J}_{\mathrm{s}n} g \mathrm{d}S_n \mathrm{d}S_m \\ &\quad - \frac{\mathrm{j}}{\omega\varepsilon} \int_{S_m} \int_{S_n} (\nabla_{\mathrm{s}} \cdot \mathbf{J}_{\mathrm{s}m})(\nabla_{\mathrm{s}} \cdot \mathbf{J}_{\mathrm{s}n}) g \mathrm{d}S_n \mathrm{d}S_m \end{aligned} \tag{67}$$

$$\begin{aligned} Z_{mn}^{\mathrm{em}} &= -\int_{S_m} \mathbf{J}_{\mathrm{s}m} \cdot \mathbf{K}(\mathbf{M}_{\mathrm{s}n}) \mathrm{d}S_m \\ &= \int_{S_m} \int_{S_n} (\mathbf{M}_{\mathrm{s}n} \times \mathbf{J}_{\mathrm{s}m}) \cdot \nabla g \mathrm{d}S_n \mathrm{d}S_m \end{aligned} \tag{68}$$

with dual expressions for magnetic/magnetic and magnetic/electric generalized impedances. These expressions can be implemented for any type of surface discretization and any adopted set of divergence-conforming basis functions in the context of the Galerkin method. In the case of using generalized curved parametric quadrilaterals in (25) in conjunction with higher order basis functions in (40)–(44), all elements of the Galerkin impedance matrix can be found as linear combinations of the following basic Galerkin potential and scalar field integrals [43]:

$$\zeta_p = \int_{-1}^{1}\int_{-1}^{1}\int_{-1}^{1}\int_{-1}^{1} u_m^{i_m} v_m^{j_m} u_n^{i_n} v_n^{j_n} g(R) \mathrm{d}u_n \mathrm{d}v_n \mathrm{d}u_m \mathrm{d}v_m \tag{69}$$

$$\zeta_f = \int_{-1}^{1}\int_{-1}^{1}\int_{-1}^{1}\int_{-1}^{1} u_m^{i_m} v_m^{j_m} u_n^{i_n} v_n^{j_n} \frac{1}{R} \frac{\mathrm{d}g(R)}{\mathrm{d}R} \mathrm{d}u_n \mathrm{d}v_n \mathrm{d}u_m \mathrm{d}v_m \tag{70}$$

where the source-to-field distance R is computed as

$$R = |\mathbf{r}_m(u_m, v_m) - \mathbf{r}_n(u_n, v_n)|. \tag{71}$$

When R is zero or small, a special treatment of singular (or nearly singular) integrals is needed. Typical FEM Galerkin integrals are those in (18). The numerical integration is practically exclusively carried out using the Gauss–Legendre integration formula.

In TDIE analysis using spatial/temporal basis functions in (51), Galerkin testing in space (over surface elements in the model) is combined with point matching at times $k\Delta t$, $k = 1, 2, \ldots, N_{\mathrm{t}}$, resulting in a set of N_{t} matrix equations of order N_{s} with $N_{\mathrm{t}}N_{\mathrm{s}}$ unknowns α, which is solved in a MOT iterative fashion [53].

To ensure that the CPU time per unknown in higher order solutions is comparable to that in low-order solutions, rapid and accurate recursive procedures are needed for evaluation of elements of MoM and FEM matrices. It is important for the efficiency of the solution that computation algorithms avoid redundant operations related to the indices for basis and testing functions [e.g., indices i and j in (69) and (70)] and for geometrical representations [e.g., indices m and n in (25)] within all of the interactions in the MoM/FEM solution, as well as the summation indices in the integration formulas. All these numerical "details" are essential for making the higher order CEM approach an efficient and practical analysis and design tool for engineers.

B. Evaluation of Singular Integrals

The techniques for dealing with singular integrals (arising for zero or small source-to-field distances) can be classified into singularity extraction or subtraction techniques and singularity cancellation or coordinate transformation techniques. The singularity extraction techniques have been traditionally used for low-order IE solutions since the first MoM implementations in analysis of wire antennas, and have been more recently accommodated for higher order IE methods [41], [71], [2], [3], [139]–[141]. Although being known for quite long time, the coordinate transformation techniques have started to gain attention in CEM since relatively recently, most notably in the various forms of the Duffy method [142]–[144], [139], [140], [50].

As an illustration of the singularity extraction (subtraction) approach, we refer to a combined numerical/analytical procedure for evaluation of potential integrals over generalized curved quadrilaterals with polynomial basis functions involved in Galerkin integrals (69) [41], [3]. It consists of analytical integration of a principal singular part of the integrand over a (generally not rectangular) parallelogram whose surface is close to the surface of the generalized quadrilateral near the singular point, and numerical integration of the rest using Gauss–Legendre quadrature formulas

$$\begin{aligned} I_{\mathrm{q}} &= \int_{-1}^{1}\int_{-1}^{1} u^i v^j g(R) \mathrm{d}u \mathrm{d}v \\ &= \int_{-1}^{1}\int_{-1}^{1} \left[u^i v^j g(R) - u_0^i v_0^j \frac{1}{4\pi R_{\mathrm{p}}} \right] \mathrm{d}u \mathrm{d}v \\ &\quad + \frac{u_0^i v_0^j}{4\pi} \int_{-1}^{1}\int_{-1}^{1} \frac{1}{R_{\mathrm{p}}} \mathrm{d}u \mathrm{d}v \end{aligned} \tag{72}$$

where u_0 and v_0 are the coordinates of the singular point. The parallelogram is defined by the unitary vectors $\mathbf{a}_u$ and $\mathbf{a}_v$ of the generalized quadrilateral, (42), at the singular point, and R_{p} is the source-to-field distance for integration over the surface of the parallelogram. Note that this technique remains practically the same when I_{q} is a near-singular integral, namely, when the projection of the observation (field) point onto the parametric surface in (25) does not belong but is close to the generalized quadrilateral (at least one of the parametric coordinates of the projection point is outside the range $-1 \leq u, v \leq 1$), in which case the singular point (u_0, v_0) is the nearest point on one of the edges of the quadrilateral.

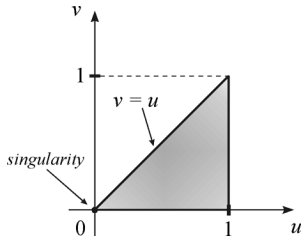

Fig. 10. Parametric u-v representation of one of the three subtriangles defined by the singular point and the vertices of a source generalized curved triangle in (31) — for evaluation of singular potential integrals in (73) using the Duffy singularity cancellation method.

As an illustration of the singularity cancellation approach [142], [50] consider potential integrals associated with interpolatory basis functions (48), on generalized curved triangles in (31). The first step is to subdivide the triangle into three subtriangles defined by the singular point and the vertices of the triangle. Each subtriangle, having the singular point as one of its vertices, is then independently represented by local parametric coordinates $0 \leq u \leq 1$ and $0 \leq v \leq u$, as illustrated in Fig. 10, using the appropriate Jacobian ($\Im$) for the transformation, so that the singularity is at the origin ($u = v = 0$). Next, a Duffy coordinate transformation $v = u\,p$ ($dv = u\,\mathrm{d}p$) is used to transform the integration to a unit square and express the source-to-field distance as $R = uR'$. Hence, the integral over the subtriangle is expressed as

$$I_{\mathrm{t}} = \int_0^1 \int_0^u \frac{f}{R} \Im \,\mathrm{d}v\mathrm{d}u = \int_0^1 \int_0^1 \frac{f}{uR'} \Im\, u\mathrm{d}p\mathrm{d}u = \int_0^1 \int_0^1 \frac{f}{R'} \Im\,\mathrm{d}p\mathrm{d}u \quad (73)$$

which removes (cancels) the singularity, since $R' \neq 0$ for all $p \in [0,\, 1]$ and $u \in [0,\, 1]$, and the integration can be carried out numerically, using quadrature formulas. Finally, the contributions of individual subtriangles are added up for the total potential integral. Note that this technique appears not to work well for near-singular integrals (when the projection point is outside the source triangle but close to it). On the other hand, the improved singularity cancellation technique in [144] accurately and efficiently handles both singular and near-singular potential integrals.

C. Higher Order Nyström Discretization

As an alternative to higher order Galerkin MoM solutions to SIEs, the Nyström method [137], [28], [32], [55]–[58] is based on a point-based discretization of the given SIE employing a higher order sampling of unknown surface currents at the abscissa points of a quadrature rule (most frequently, the Gauss-Legendre rule) over curvilinear surface elements, as in (53) or (54), and point-matching testing procedure at the same points. The scattered electric field sample at the ith quadrature point on the mth surface element (field matching point), the position vector of which is $\mathbf{r}_{mi}$, has the following form:

$$E(m,n,i,j) = \sum_{n=1}^{N_{\mathrm{e}}} \sum_{j=1}^{P_n} w_{nj} G(\mathbf{r}_{mi}, \mathbf{r}_{nj}) J_{\mathrm{s}}(\mathbf{r}_{nj}) \quad m = 1, 2, \ldots, N_{\mathrm{e}}, \quad i = 1, 2, \ldots, P_m \quad (74)$$

where G is the integral kernel of the SIE, N_{e} the total number of elements in the model, P_m (P_n) the number of quadrature points on the mth (nth) element, and $\mathbf{r}_{nj}$ and w_{nj}, respectively, the abscissa (position vector) and weight of the jth quadrature point on the nth element (source point). This leads to a square system matrix with current samples as unknowns.

The higher order accuracy of the Nyström method in (74) can be achieved only with a proper treatment of singularities in the kernel G, leading to locally corrected Nyström (LCN) schemes. In LCN techniques [28], [32], [55]–[57], the impedance matrix is locally corrected in regions where the source-to-field distance is small (or zero) using specialized (adjusted) quadrature rules that integrate singular kernels to high order, whereas simple single-point evaluations of G suffice for the remaining matrix entries. This is why the system matrix fill time for a higher order LCN method is dramatically reduced when compared to the corresponding Galerkin MoM. The corrected weights for the specialized local quadrature rule are derived from a MoM procedure. A higher order LCN scheme with a local correction based on the Lagrange interpolation of the unknown function and singularity extraction and Duffy transformation for singular kernels is also developed [58].

D. Higher Order MLFMA and PWTD Techniques

Using the multilevel fast multipole algorithm (MLFMA), the memory requirements and computational complexity of the large-scale MoM can be reduced from $O(N_{\mathrm{un}}^2)$ to $O(N_{\mathrm{un}} \log N_{\mathrm{un}})$, where N_{un} is the total number of unknowns in the model [5]. This acceleration is achieved by taking advantage of small or negligible coupling between the currents on nonadjacent and especially very distant surface elements in the model, and is essentially based on breaking the IE interaction matrix into near and far zone sections based on the distance between testing and source locations

$$[Z] = [Z]^{(\mathrm{near})} + [Z]^{(\mathrm{far})} \quad (75)$$

and introducing appropriate simplifications and approximations in treating the far zone interactions at different levels. More specifically, while the sparse matrix $[Z]^{(\mathrm{near})}$ is computed explicitly in a standard MoM fashion, $[Z]^{(\mathrm{far})}$ is computed implicitly, using the multipole expansion of Green's function. The procedure consists of grouping the basis functions and expressing the interaction between groups by a translation operator, which speeds up the matrix-vector multiplication in the iterative solution of the MoM matrix equation. Furthermore, the algorithm is recursively organized across multiple levels, by grouping smaller groups into larger ones, and reusing the translation operator to compute the interactions between groups at each level.

The MLFMA can be used to accelerate the solution of higher order Galerkin-type MoM, as in the MLFMA-accelerated SIE technique employing higher order interpolatory divergence-conforming basis functions (48) on generalized curved triangular patches [50]. However, in such arrangements, implementing higher order discretizations to reduce the number of unknowns and MLFMA to reduce the computational complexity, as the two general approaches to enhance the efficiency

of the MoM and reduce the CPU time and memory requirements, are somewhat contradictory. Namely, since the number of levels in the MLFMA is determined by the size of elements in the model, the use of large elements associated with the use of higher order basis functions implies the reduction of the number of levels and thus limited performance of the higher order MLFMA in conjunction with Galerkin-type solutions. A remedy here is to use point-based higher order basis functions, such as those in (53) or (54), which is equivalent to replacing a continuous current distribution by point sources (samples), and the associated point-matching testing, which can be interpreted as a reduction of the Galerkin-based formulation to a Nyström-type discretization. The MLFMA is applied to calculate the point-to-point interactions, rather than the standard basis-to-basis MoM interactions [47]. Since the point bases have no spatial extent, the number of levels in the MLFMA can be made the same as with low-order Galerkin solutions, e.g., if using RWG basis functions in (45).

On the other side, the TDIE solutions can be accelerated by the multilevel plane-wave time-domain (PWTD) algorithm [145], which is the time-domain counterpart of the MLFMA (in the frequency domain). The reduction in the computation complexity with the PWTD, analogous to that with the MLFMA, is achieved, in far zone interactions, through expansion of transient fields radiated by temporally bandlimited surface currents in terms of a discrete set of time-gated uniform plane waves that is characterized by a diagonal translation operator. In [97], the multilevel PWDT scheme is applied to accelerate the BI part of the higher order TD-FE-BI technique, formulated in (22).

E. Matrix Solvers

In all described classes of higher order CEM techniques, the resulting system of linear equations is solved using either direct solvers, such as those based on the Gaussian elimination or lower–upper (LU) decomposition, for relatively small problems in terms of the required number of unknowns ($N_{\rm un}$) or iterative solvers, like those based on the conjugate gradient (CG) method [146], for large problems. Some of the extensively used iterative solvers are the biconjugate gradient stabilized (BiCGStab) [147], conjugate gradient squared (CGS) [148], generalized minimum residual (GMRES) [149], and transpose-free quasi-minimum residual (TFQMR) [150] methods. In MoM, the computation time for the solution is proportional to $N_{\rm un}^3$ with direct solvers, to $N_{\rm un}^2$ with iterative solvers, or to $N_{\rm un}\log N_{\rm un}$ with accelerated iterative solvers (e.g., MLFMA-accelerated solvers). With higher order discretizations, however, $N_{\rm un}$ can be quite small even for electrically relatively large problems, so that direct solvers suffice for a variety of practical applications. In FEM, the matrices are sparse, and hence sparse direct solves, such as the multifrontal method [151], and sparse iterative solvers, usually based on the CG method, are used. In addition, by only storing the nonzero entries, the memory requirements in FEM can be reduced from $O(N_{\rm un}^2)$ to $O(N_{\rm un})$. For both MoM and FEM techniques, as well as hybrid solutions, the convergence rate of iterative solvers can be greatly enhanced employing appropriate preconditioners. Some of the routinely utilized preconditioners in CEM are incomplete LU (ILU), sparse approximate inverse (SPAI), and block Jacobi preconditioners [152].

F. Code Validation and Error Estimates

In addition to various standard verification and validation tests of the results obtained by a newly developed numerical technique and code, against analytical results, results obtained by other numerical methods, and experimental results, in higher order CEM the principal attention must be paid to numerical convergence properties of the solution. Namely, it must be verified that the computed results for different quantities converge (the error in the computed solution decreases) rapidly and smoothly to the correct answer as the current/field approximation orders are increased and the discretization scales (element sizes) are decreased. Assuming a uniform discretization over the entire structure, defined by the element size h (the same in all dimensions), for very small values of h (theoretically, in the limit of $h \to 0$) the error (for different error measures) should in general scale asymptotically as $O(h^p)$, where p is the order of convergence of the method that increases with the current/field approximation orders in the model; large values of p mean a high-order algorithm. Moreover, convergence properties of the solution in terms of higher geometrical orders of elements for surfaces with pronounced curvature need to be tested. Sometimes, in cases when analytical, experimental, or numerical (already verified) reference results are not available, the error of a particular computed solution is given taking the "best" result by the technique under test (e.g., with extremely high current/field approximation orders and/or overly fine mesh) as the "correct" answer.

Along with benchmarking, i.e., numerical validations of the code using collections of test cases, accuracy and convergence properties of the method can be assessed, in some cases, by means of theoretical error estimates [153]–[159]. Ideally, the theoretical error analysis of the CEM algorithm employed and the problem under consideration should provide a general proof that the numerical solution converges to the exact solution as the model is refined, and enable a quantification of the solution error in terms of the numerical parameters of the algorithm (types of the geometrical elements and basis functions, discretization density, current/field approximation orders, quadrature rule orders, iteration counts, etc.) and physical properties of the problem (electrical size, shape, and material composition of the structure, excitation, etc.). Although quantitative error estimates in CEM are currently available only for problems of quite limited scope (mostly canonical problems) [154]–[159] and are seldom given for higher order property of the solution [153], [155], they are much needed and very useful, as they not only place a CEM technique on solid theoretical ground, but also offer important conclusions on the accuracy and convergence behavior of the technique that can often be extrapolated to more general problems of practical interest. For instance, such estimates may provide theoretical understanding of factors that cause solution errors in simulations, as well as theoretical insights into error trends obtained from empirical numerical observations (benchmarking). CEM error analysis also includes *a posteriori* residual error estimates (available

after the numerical analysis of the problem) [160], [161], used in adaptive algorithms.

Ultimately, the goal is to create as precise as possible quantitative (theoretical or empirical) recipes for "dialing" accuracy of the solution, i.e., for determining minimal current/field expansion orders and other numerical parameters of the model needed for the specified level of desired accuracy or acceptable uncertainty of the results in practical implementations. Additionally, explicit tradeoffs between accuracy and efficiency, i.e., the cost of getting the results, should be established and made accessible to the CEM modeler.

G. Adaptive Higher Order Solutions

The accuracy of an existing CEM solution to a given problem can be improved by refining the mesh (h-refinement), increasing the current/field approximation orders over elements without subdividing the elements (p-refinement), or combining the two approaches (hp-refinement). Of course, p- and hp-refinements are possible only with higher order basis functions. In adaptive CEM schemes, the solution is refined step by step, automatically, according to an error indicator. Interpolatory divergence- or curl-conforming higher order bases are not suitable for p-based adaptions, since they do not allow selective p-refinement (orders of current/field approximation must be the same in all interpolatory elements). Hierarchical higher order techniques enable not only selective variation of current/field approximation orders and element sizes throughout the mesh to optimize the model performance but also efficient systematic updating of MoM and FEM matrices in the adaption process, where the matrix at each step consists of the old entries for lower orders, which are already known from the previous step, and new entries for the increased orders.

The error indicators are most frequently *a posteriori* error estimates, computed from the existing numerical solution at each step. For instance, one can use the residual of (17) to estimate the error over each element in an FEM discretization [10], or check power conservation within the structure under consideration [162]. Local errors in numerically satisfying different continuity boundary conditions across edges/sides shared by adjacent surface/volume elements in the model can also be used.

Within the IE framework, an example of adaptive solutions is a p-adaptive hierarchical MoM technique for SIE analysis of PEC structures using divergence-conforming curvilinear triangular meshes in [37], where the numerical discontinuity of the tangential component of the current density vector $\mathbf{J}_{\mathrm{s}}$ on common edges between elements is implemented as an *a posteriori* error indicator (normal component of $\mathbf{J}_{\mathrm{s}}$ is continuous in any numerical solution due to divergence-conformity of the basis functions). On the other side, as an example of DE (and hybrid) adaptive algorithms, we refer to an hp-adaptive higher order hierarchical tetrahedral FE-BI technique in [117], where the selective assignment of new element sizes and/or polynomial orders is based on *a posteriori* error estimates for individual elements, in order to reduce the global error uniformly throughout the mesh. The element error is estimated separately for the electric and magnetic fields, via their respective energies within the element, namely, the element energy integrals of the error-indication electric and magnetic fields, defined as the difference of $\mathbf{E}$ when computed directly (by the FE-BI code) and indirectly from the direct solution for $\mathbf{H}$ and Ampère's law, and vice versa for the magnetic energy integral.

H. Higher Order Meshing Techniques

Since higher order geometrical elements are much more complex and flexible in shapes and sizes than the low-order ones, generation of optimal meshes for practical 3-D electromagnetic problems based on any particular class of higher order finite or boundary elements is a difficult and challenging task. Most frequently, higher order meshes (with curvilinear elements) are generated starting from low-order meshes (with flat surface elements or flat-sided volume elements), and then *a posteriori* adapting (curving) them by placing additional points at the curved edges and surfaces describing the actual geometry [163], [164]. An alternative approach is direct higher order mesh generation, as in a quadrilateral surface meshing technique using a recursive decomposition of the domain into polygonal shapes (templates), and then meshing the polygons into a minimum number of connected bilinear quadrilaterals (27) [165]. Another example is a semi-automatic algorithm for the higher order large-domain hexahedral mesh generation that represents a combination of the domain decomposition and mapped meshing techniques [166], where a parametric mesh of topologically equivalent elements with correct connections is created first (based on the problem topology and adopted orders of elements), and parts of the structure are then mapped from the parametric space to the curved hexahedral elements (35) in the real 3-D space. These forms (sub-meshes) are connected together appropriately into an optimal large-domain mesh that can be further refined if necessary.

VI. Numerical Examples

As the first numerical example of higher order CEM modeling, consider the convergence of the results for the bistatic scattering cross section (BCS) of a spherical PEC scatterer of radius 4.5λ. The results obtained by a higher order MLFMA-accelerated MoM solution [50] to the CFIE in (4) using divergence-conforming interpolatory basis functions (48), on generalized curved triangles in (31), are compared with the analytical solution in the form of Mie's series. Fig. 11 shows the rms error in the BCS over a number of observation angles as a function of the number of unknowns per wavelength squared, for both E- and H-planes [50]. The results are obtained using several different (refined) meshes of the sphere (h-refinement), with different (refined) orders of basis functions (p-refinement) in individual meshes. We observe a dramatic improvement in the convergence and efficiency of the solution when using higher order bases. The advantage of higher order solutions is particularly pronounced when a higher accuracy is desired. For instance, the total numbers of unknowns in the model to obtain a solution with the rms BCS error less than 0.2 dB in the E-plane amount to about 43 200, 9600, and 7000 with zeroth-, first-, and second-order basis functions, respectively. On the other side, the corresponding numbers of unknowns for a 0.1 dB rms accuracy are about 80 688, 14 440, and 8400. In this latter case, the mesh

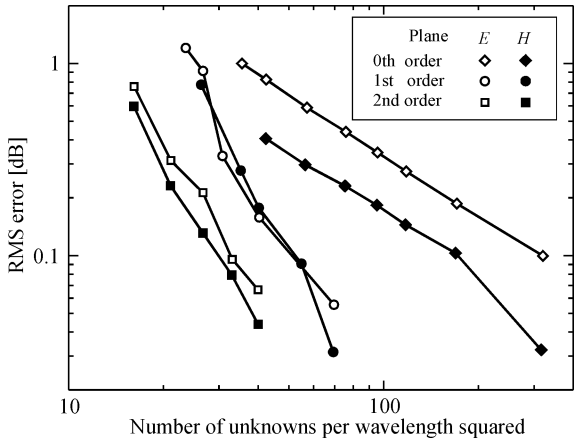

Fig. 11. RMS error in the bistatic scattering cross section of a spherical PEC scatterer of radius 4.5λ, as a function of the number of unknowns per wavelength squared, computed by higher order MLFMA-accelerated MoM solution to (4) using basis functions (48) on elements (31) and several meshes (h-refinement) with different orders of basis functions (p-refinement) [50].

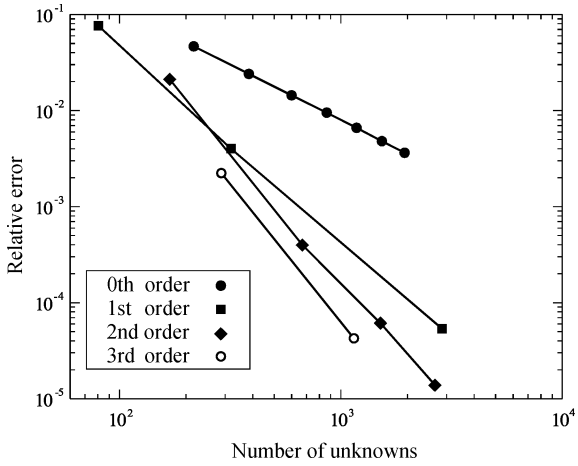

Fig. 12. RMS error versus the total number of unknowns in the BCS of a dielectric spherical scatterer with relative permittivity $\varepsilon_{\rm r} = 2.6$ and radius 0.25λ computed by the MLFMA SIE discretization of (6) and (7) with $\alpha = \beta = 1$ using the same elements and bases and similar h- and p-refinements as in Fig. 11 [52].

densities are about 330, 55, and 33 unknowns per λ^2 using the zeroth-, first-, and second-order basis functions, respectively.

The next example illustrates the higher order convergence of the MLFMA technique [52] applied to a SIE model for arbitrary material structures with the PMCHWT ($\alpha = \beta = 1$) version of (6) and (7), triangular patches in (31), and interpolatory bases in (48). In a similar numerical experiment to that in Fig. 11, shown in Fig. 12 is the rms error in the simulated BCS of a dielectric spherical scatterer (taking the Mie's series solution as a reference) with the relative permittivity $\varepsilon_{\rm r} = 2.6$ and radius 0.25λ versus the total number of unknowns in the model [52]. Again, a dramatic improvement in accuracy and convergence properties of the solutions when using higher order basis functions is observed, with the improvement being more pronounced if a higher accuracy is required.

Next, the numerical advantages of a higher order TD-FEM discretization of (22) using spatial/temporal field expansion in (63) [97], with curl-conforming interpolatory spatial bases (62)

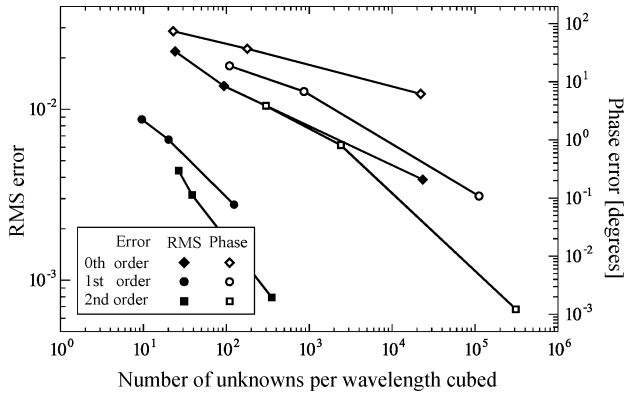

Fig. 13. RMS error and phase error, against the number of unknowns per wavelength cubed, in computing the total field near a PEC sphere illuminated by a Neumann pulse using a higher order TD-FEM discretization of (22) with basis functions (62)–(63) on elements (38), and h- and p-refinements [97].

on generalized curved tetrahedra in (38), are illustrated on an example of a PEC sphere, 1 m in radius. The incident wave is a Neumann pulse with the maximum frequency $f_{\max} = 1.5$ GHz (and the corresponding minimum wavelength $\lambda_{\min} = 0.2$ m), and a PWDT-accelerated TD-FE-BI scheme is applied [97]. The computations are carried out using three FEM meshes around the sphere with the average edge length of tetrahedral elements equal to $0.1\lambda_{\min}$, $0.5\lambda_{\min}$, and $1\lambda_{\min}$, respectively, and zeroth-, first-, and second-order basis functions for each mesh. Fig. 13 shows the normalized rms error and the accumulated phase error for the component of the total electric field with the same polarization as the incident field observed at a near-field point of the sphere (compared to the exact Mie's solution), plotted against the number of unknowns per the wavelength cubed [97]. We clearly observe the higher order convergence of the results due to the use of bases in (62). In addition to the achieved accuracy and enhanced convergence rate of the field amplitude calculation, the well known problem of phase error accumulation using low-order (zeroth-order) FEM schemes, which severely impedes the analysis of late time responses, is effectively mitigated using higher order elements.

As an illustration of numerical benefits of using the higher order Nyström methodology, consider a higher order Nyström scheme for PEC structures [58], based on the SIE discretization in (74) and point-based basis functions (54) on generalized triangular patches. Fig. 14 presents the rms error in the simulated radar cross section (RCS) in the *HH* polarization, based on the EFIE in (1), of a PEC ogive scatterer whose geometry is shown in the figure inset with $a = 1$ in and $d = 5$ in at the frequency $f = 1.18$ GHz, as a function of the number of unknowns per wavelength [58]. The results are given for five different (h-refined) meshes of the structure, and three different (p-refined) Gauss–Legendre quadrature rules, namely, the second-, third-, and fourth-order rules, respectively, according to [167], for each mesh. The reference solution corresponds to a very fine discretization of the geometry (360 patches) and the highest-order quadrature rule, resulting in a total of 2160 unknowns (or 71.6 unknowns per wavelength). The error curves clearly demonstrate the higher order convergence of the solution, with the error being reduced at a much higher rate as the mesh is refined,

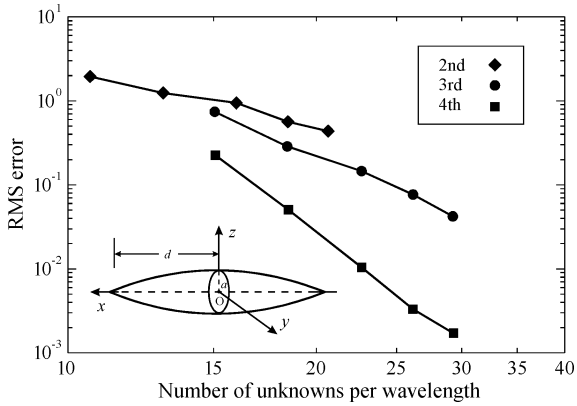

Fig. 14. RMS error in the radar cross section (*HH* polarization) of a PEC ogive scatterer shown in the inset ($a = 1$ in, $d = 5$ in, $f = 1.18$ GHz), versus the number of unknowns per wavelength, computed by a higher order Nyström scheme based on (1) and (74) with basis functions (54) on elements (31), using different (h-refined) meshes and different (p-refined) Gauss–Legendre quadrature rules [58].

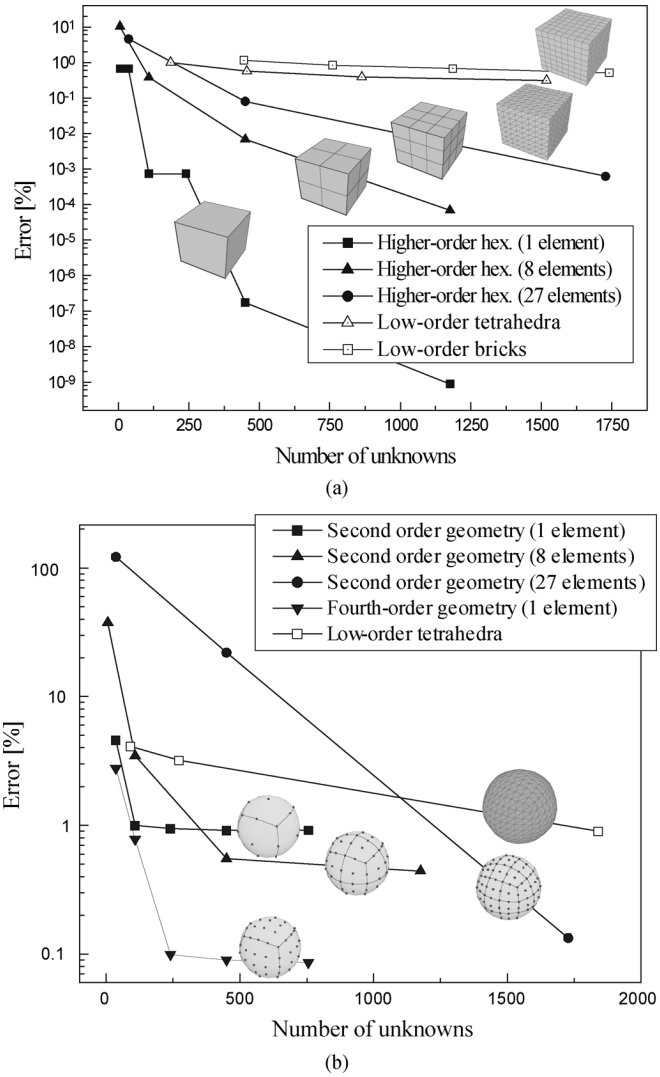

Fig. 15. Error in k_0 of the dominant degenerate eigenmodes of (a) a cubical cavity and (b) a spherical cavity, against the number of unknowns, computed by a higher order hierarchical FEM discretization of (18) using elements (35) and basis functions (60), for several higher order models [102]. Results using low-order models in [168] (for the cubical cavity) and [169] (for the spherical cavity) are also shown [102].

if higher order quadrature rules, or, equivalently, higher order point-based basis functions, are used.

To illustrate the advantages of higher order hierarchical FEM modeling, we consider a discretization of (18) [102] using generalized hexahedral elements in (35) and curl-conforming hierarchical basis functions in (60), as applied to eigenvalue analysis of electromagnetic cavities. Fig. 15(a) shows the error (with respect to the analytical solution) in calculating k_0 of the dominant degenerate eigenmodes of a cubical cavity against the number of unknowns, for three higher order models [102] and two low-order models [168]. In the first higher order solution, the cavity is represented by a single trilinear hexahedron with the field-expansion orders being varied from 2 to 7 (p-refinement). Note that this is literally an entire-domain FEM model (an entire computational domain is represented by a single finite element). The other two higher order solutions are shown to indicate the model behavior when the number of elements is increased as well, which corresponds to an h-refinement of the model. We observe great superiority of higher order FEM solutions. Fig. 15(b) shows a similar analysis for a spherical cavity, where the analytical solution is available as well. Here, the number of unknowns for 1% accuracy with the low-order model [169] (1840) is 17 times that (108) with both single-element (entire-domain) curvilinear models. We also note that it is impossible to p-refine the single-element model of the second geometrical order (with a triquadratic hexahedron) below about 1% error, whereas approximately 0.1% accuracy can be achieved using as little as 240 unknowns with a single-element model of the fourth geometrical order. In turn, more than 1728 unknowns and at least 27 elements are necessary for getting the same level of accuracy with the second-order geometrical modeling.

For an additional insight into h- and p-refinements in conjunction with higher order hierarchical FEM simulations, Fig. 16 shows the convergence of the results for the effective dielectric constant of a circular waveguide computed by a 2-D FEM technique [105] using curl-conforming hierarchical expansion (55) on generalized quadrilaterals in (25) and taking the analytical solution as the reference. The points on the broken line correspond to h-refined solutions with low-order bases, using meshes with 1, 5, 12, 48, and 320 elements, respectively, as indicated in the figure inset; the points on the solid lines are obtained by p-refining the respective initial models. It can be observed that, in this example, the p-refinement represents a better choice in terms of achieving a certain level of accuracy with lesser computation cost. However, the figure also shows that an arbitrarily high accuracy cannot be achieved by performing the p-refinement alone; instead, a combined hp-refinement should be utilized in order to obtain an optimal modeling performance. This conclusion holds generally, in a sense that there exists a low-error bound beyond which a p-refinement in arbitrarily coarse meshes does not improve further the accuracy of the solution and the size of elements needs to be reduced as well. Another 2-D FEM example [105] is a simulation of two coupled microstrip lines on a cylindrical

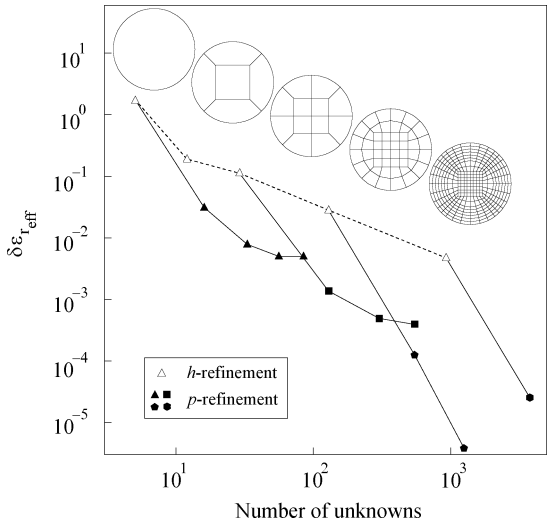

Fig. 16. Error in the effective dielectric constant averaged for the four dominant modes of a circular waveguide, against the number of unknowns, computed by a 2-D FEM technique using basis functions (55) on elements (25), with h- and p-refinements [105].

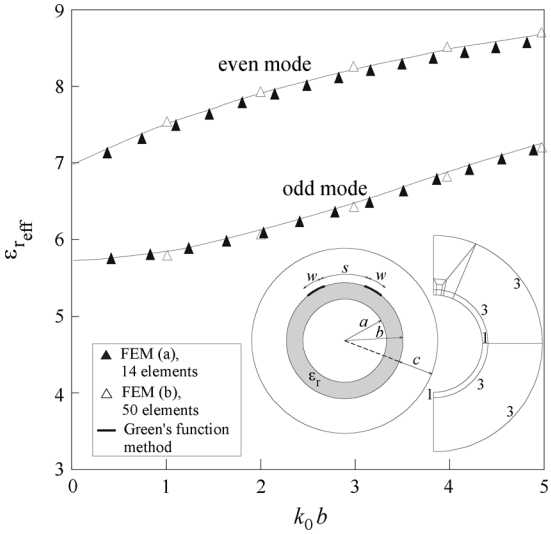

Fig. 17. Dispersion curves of two coupled microstrip lines on a cylindrical substrate, the cross section of which is shown in the inset ($a/b = 0.9, c/h = 10, s/h = 1, w/h = 1, h = b - a, \varepsilon_r = 9.6$), computed by the 2-D FEM technique used in the analysis in Fig. 16 [FEM (a)], with a 14-element quadrilateral mesh also shown in the inset with designated field-approximation orders (where not shown, the adopted order is 2) [105]; FEM results [FEM (b)] from [82] and solution using Green's function method [170] are also shown [105].

substrate using a 14-element higher order mesh consisting of both large and small elements of very different shapes, as depicted in Fig. 17, which illustrates the flexibility of mesh generation provided by higher order hierarchical bases.

The next example uses a higher order Galerkin MoM solution [43] to the EFIE in (1) with divergence-conforming hierarchical basis functions in (40) and (41), defined on generalized curved quadrilaterals in (25), to illustrate the advantages of combining higher order geometrical modeling and higher order hierarchical current modeling in SIE computations. Fig. 18 depicts three geometrical models of a spherical PEC scatterer using bilinear quadrilaterals in (27) in conjunction with the second-order current approximation and two geometrical models using quadrilaterals of the fourth geometrical order in (28) with the eighth-

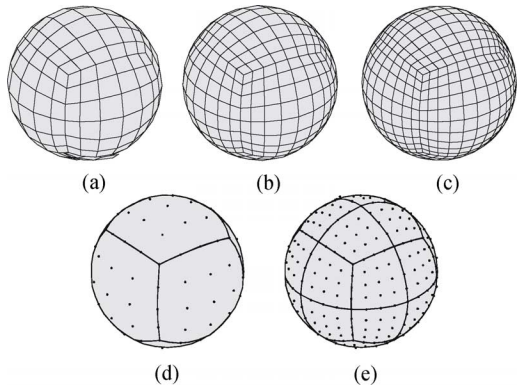

Fig. 18. Three geometrical models of a spherical PEC scatterer constructed from (a) 216, (b) 384, and (c) 600 bilinear quadrilaterals in (27) and two models constructed from (d) 6 and (e) 24 generalized quadrilaterals of the fourth geometrical order in (28) [43].

and sixth-order current approximation for 6- and 24-element models, respectively [43]. The total numbers of unknowns for models (a)–(e) amount to 1728, 3072, 4800, 768, and 1728, respectively. From Fig. 19(a), showing the simulated RCS of the sphere using models (a)–(c) in Fig. 18, we observe a good agreement between the numerical results obtained with model (c) and analytical results (Mie's series) in the entire frequency range considered, whereas models (a) and (b) provide acceptable results only at lower frequencies. Note that an increase in the current-approximation orders in models (a) and (b) does not yield better results at higher frequencies, meaning that the errors in the RCS prediction are a consequence of the inaccuracy in geometrical modeling of the sphere surface. In Fig. 19(b), a good performance of model (d) is observed up to the frequency at which the curved quadrilateral elements in the model are approximately 2λ across, while model (e) agrees well with the exact solution at all frequencies. Generally, optimal modeling is achieved by keeping the elements as large as possible – of course, within certain limits. Based on this and many other numerical experiments across different higher order techniques, a length of 1.5λ can be adopted to be the maximal dimension of elements and the general limit in the CEM procedure beyond which the structure is subdivided into smaller elements (note that the corresponding low-order limit is 0.1λ).

We next present the analysis of a parabolic reflector antenna with a pyramidal horn feed, shown in the inset of Fig. 20, using a higher order hierarchical MoM-PO technique for solving the EFIE/MFIE system in (1) and (16) [44], to illustrate the efficiency of a hybridization of a numerically rigorous method (MoM) and asymptotic high-frequency technique (PO) in a higher order computational framework. The reflector is modeled by 420 generalized quadrilaterals (25) of the second geometrical order, that are between 0.88λ and 1.11λ on a side. The total number of unknowns using the two-fold symmetry of the problem is 5458. The simulated co-polarization normalized pattern in the 45-degree plane is shown in Fig. 20 [44], where an excellent agreement of the MoM-PO results (horn in the MoM region, reflector in the PO region) and pure MoM results

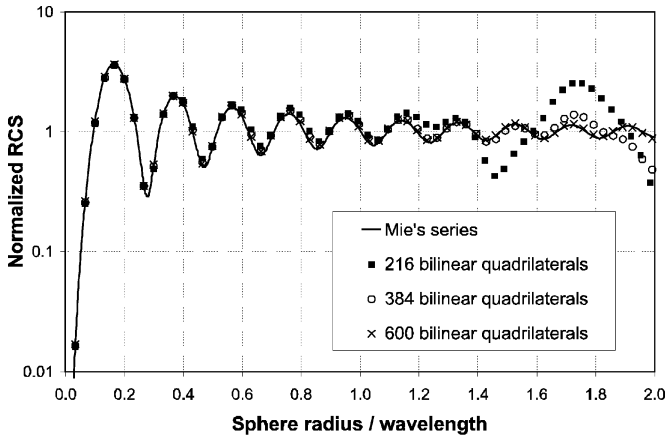

Fig. 19. Normalized radar cross section of a PEC sphere computed by a higher order Galerkin MoM solution to (1) with basis functions (40)–(41) on elements (25), for (a) models with first-order geometrical approximation in Fig. 18(a)–(c) and (b) models with fourth-order geometrical approximation in Fig. 18(d)–(e) [43].

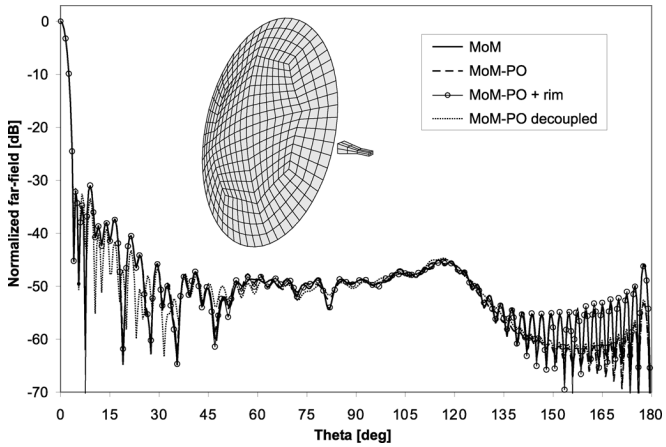

Fig. 20. Normalized co-polarization far-field pattern in the 45-degree plane of a parabolic reflector antenna with a pyramidal horn feed (shown in the inset) computed by a higher order hierarchical MoM-PO technique based on (1) and (16) using (A) the full MoM, (B) the MoM-PO with the horn in the MoM region and the reflector in the PO region, (C) the MoM-PO with a rim of MoM patches added around the reflector edge, and (D) the "decoupled" version of the MoM-PO [44].

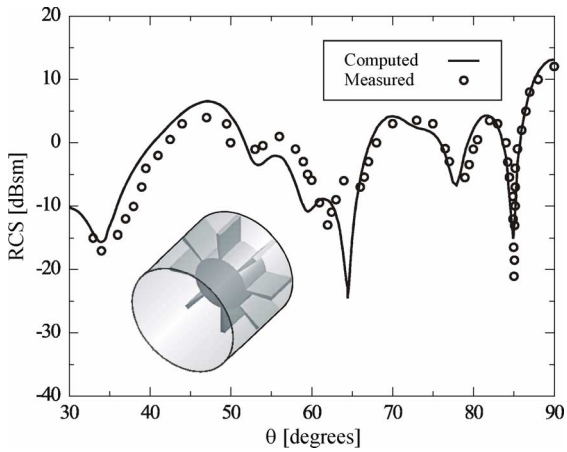

Fig. 21. Higher order FEM simulation of jet engine inlet scattering: comparison of the RCS ($\phi\phi$-polarization) of an inlet model shown in the inset (inlet depth and diameter are both 8λ) computed using third-order interpolatory tetrahedra (62) [95], for a range of incidence angles, with measured data [95].

is observed, with the only considerable disagreements occurring in the deep shadow region behind the reflector (which can be overcome by introducing a rim in the form of a single layer of MoM patches along the reflector edge). However, the hybrid analysis is more than 25 times faster than the full MoM analysis. Note also that the low-order technique with RWG basis functions and the use of two-fold symmetry would require more than 33 000 unknowns for the same problem.

The last example illustrates the effectiveness of higher order tetrahedral FEM modeling in frequency-domain scattering simulations, as applied to analysis of scattering by jet engine inlets [95]. Fig. 21 shows the RCS ($\phi\phi$-polarization) of an engine inlet model (shown in the figure inset) in the form of a circular metal-backed cavity loaded by an array of straight blades mounted radially on a cylindrical hub (inlet depth and diameter are both 8λ), for a range of incidence angles (θ). The discretization of the inlet interior using third-order interpolatory curl-conforming tetrahedral finite elements in (62), with a BI closure across the inlet aperture, results in a total of 319 728 unknowns, and requires very reasonable computational resources [95]. We observe a very good agreement of the computed RCS with measured data.

VII. Conclusion

This paper has reviewed the higher order computational electromagnetics for antenna, wireless, and microwave engineering applications. These CEM techniques use higher order current/field basis functions defined on large (e.g., on the order of λ in each dimension) curvilinear geometrical elements, which greatly reduces the number of unknowns for a given problem and enhances the accuracy and efficiency of the analysis. Focusing on frequency-domain techniques, the paper has presented all major surface/volume integral- and differential-equation electromagnetic formulations within a higher order computational framework, including SIE formulations for PEC and arbitrary material structures, respectively, VIE and VSIE formulations, SIE-Green's function formulations for multilayer media, hybrid MoM-PO formulations, and FEM, FE-ABC, and FE-BI formulations. With a systematic and as unified and consistent as possible review of generalized curved parametric quadrilaterals, triangles, hexahedra, and tetrahedra used for higher order geometrical modeling and various types

of higher order hierarchical and interpolatory vector basis functions, in both divergence- and curl-conforming formats, used for current/field modeling, a large number of actual higher order techniques, representing various combinations of formulations, elements, and bases, have been identified and discussed. In addition, several important components of the higher order solution have been addressed, including testing procedures, evaluation of singular integrals, Nyström discretization, MLFMA and PWTD accelerations, matrix solvers, error estimates, h-, p-, and hp-refinements and adaptive schemes, and mesh generation.

Numerical examples have demonstrated the accuracy, efficiency, and versatility of higher order CEM techniques, and their advantages over low-order discretizations. The results have shown a much faster convergence of the solution, with increasing the number of unknowns, when higher order bases are used. It has been demonstrated that both components of the higher order modeling, namely, higher order geometrical modeling and higher order current/field modeling, are essential for accurate and efficient CEM analysis of general antenna, scattering, and microwave structures.

The paper has shown a great diversity of higher order formulations, elements, bases, and solution techniques. Although all these components, as well as their many working combinations resulting in higher order CEM codes, seem to be completely different, they all have a lot in common. On the other side, they all show some advantages and deficiencies. The choice of the "best" method depends on the particular problem that needs to be solved. Therefore, all presented and/or referenced higher order formulations, elements, bases, and solutions are important and constitute a body of knowledge in this area. Moreover, it is likely that practically all future CEM techniques and codes will have some higher order properties, because such elements and bases exhibit excellent convergence, flexibility, and suitability for refinements and adaptive simulations. Finally, low-order modeling approach is actually included in the higher order modeling.

REFERENCES

[1] R. F. Harrington, *Field Computation by Moment Methods*, ser. Electromagnetic Waves. Piscataway, NJ: IEEE Press, 1993.

[2] B. D. Popovic and B. M. Kolundzija, "Analysis of metallic antennas and scatterers," in *IEE Electromagnetic Wave Series*. London, U.K.: IEE, 1994, no. 38.

[3] B. M. Kolundzija and A. R. Djordjević, *Electromagnetic Modeling of Composite Metallic and Dielectric Structures*. Norwood, MA: Artech House, 2002.

[4] A. F. Peterson, *Mapped Vector Basis Functions for Electromagnetic Integral Equations*. San Rafael, CA: Morgan & Claypool, 2006.

[5] *Fast and Efficient Algorithms in Computational Electromagnetics*, W. C. Chew, J.-M. Jin, E. Michielssen, and J. Song, Eds. Norwood, MA: Artech House, 2001.

[6] J. M. Jin, *The Finite Element Method in Electromagnetics*, 2nd ed. New York: Wiley, 2002.

[7] P. P. Silvester and R. L. Ferrari, *Finite Elements for Electrical Engineers*, 3rd ed. Cambridge, U.K.: Cambridge Univ. Press, 1996.

[8] J. L. Volakis, A. Chatterjee, and L. C. Kempel, *Finite Element Method for Electromagnetics*. New York: IEEE Press, 1998.

[9] J. L. Volakis, K. Sertel, and B. C. Usner, *Frequency Domain Hybrid Finite Element Methods in Electromagnetics*. San Rafael, CA: Morgan & Claypool, 2006.

[10] M. Salazar-Palma, T. K. Sarkar, L. E. Garcia-Castillo, T. Roy, and A. Djordjević, *Iterative and Self-Adaptive Finite Elements in Electromagnetic Modeling*. Norwood, MA: Artech House, 1998.

[11] A. Taflove and S. C. Hagness, *Computational Electrodynamics: The Finite-Difference Time-Domain Method*, 3rd ed. Norwood, MA: Artech House, 2005.

[12] *Advances in Computational Electrodynamics: The Finite-Difference Time-Domain Method*, A. Taflove, Ed. Norwood, MA: Artech House, 1998.

[13] C. Christopoulos, *The Transmission-Line Modeling Method: TLM*, ser. Electromagnetic Waves. Piscataway, NJ: IEEE Press, 1995.

[14] W. J. R. Hoefer, "The transmission line matrix (TLM) method," in *Numerical Techniques for Microwave and Millimeter-Wave Passive Structures*, T. Itoh, Ed. New York: Wiley, 1989.

[15] M. Krumpholz and P. Russer, "A field theoretical derivation of TLM," *IEEE Trans. Microw. Theory Tech.*, vol. 42, no. 9, pp. 1660–1668, Sep. 1994.

[16] M. Krumpholz and L. P. B. Katehi, "MRTD: New time domain schemes based on multiresolution analysis," *IEEE Trans. Microw. Theory Tech.*, vol. 44, no. 4, pp. 555–561, Apr. 1996.

[17] A. Alighanbari and C. D. Sarris, "Dispersion properties and applications of the Coifman scaling function based S-MRTD," *IEEE Trans. Antennas Propag.*, vol. 54, no. 8, pp. 2316–2325, Aug. 2006.

[18] A. Alighanbari and C. D. Sarris, "An unconditionally stable Laguerre-based S-MRTD time-domain scheme," *IEEE Antennas Wireless Propag. Lett.*, vol. 5, pp. 69–72, Dec. 2006.

[19] T. Weiland, "Time domain electromagnetic field computation with finite difference methods," *Int. J. Numerical Modelling: Electronic Networks, Devices and Fields*, vol. 9, pp. 295–319, 1996.

[20] M. Clemens and T. Weiland, "Discrete electromagnetism with the finite integration technique," *Progress Electromagn. Res. (PIER)*, vol. 32, pp. 65–87, 2001.

[21] B. D. Popovic, "Polynomial approximation of current along thin symmetrical cylindrical dipoles," *IEE Proc.*, vol. 117, pp. 873–878, 1970.

[22] P. Silvester, "A general high-order finite element waveguide analysis program," *IEEE Trans. Microw. Theory Tech.*, vol. MTT-17, no. 4, pp. 204–210, Apr. 1969.

[23] D. L. Knepp and J. Goldhirsh, "Numerical analysis of electromagnetic radiation properties of smooth conducting bodies of arbitrary shape," *IEEE Trans. Antennas Propag.*, vol. AP-20, no. 3, pp. 383–388, May 1972.

[24] J. M. Jin, K. C. Donepudi, J. Liu, G. Kang, J. M. Song, and W. C. Chew, "High-order methods in computational electromagnetics," in *Fast and Efficient Algorithms in Computational Electromagnetics*, W. C. Chew, J.-M. Jin, E. Michielssen, and J. Song, Eds. Norwood, MA: Artech House, 2001.

[25] R. D. Graglia, D. R. Wilton, and A. F. Peterson, "Higher order interpolatory vector bases for computational electromagnetics," *IEEE Trans. Antennas Propag.*, vol. 45, no. 3, pp. 329–342, Mar. 1997.

[26] S. Wandzura, "Electric-current basis functions for curved surfaces," *Electromagnetics*, vol. 12, no. 1, pp. 77–91, 1992.

[27] L. R. Hamilton, J. J. Ottusch, M. A. Stalzer, R. S. Turley, J. L. Visher, and S. M. Wandzura, "Numerical solution of 2-D scattering problems using high-order methods," *IEEE Trans. Antennas Propag.*, vol. 47, no. 4, pp. 683–691, Apr. 1999.

[28] L. F. Canino, J. J. Ottusch, M. A. Stalzer, J. L. Visher, and S. M. Wandzura, "Numerical solution of the Helmholtz equation in 2D and 3D using a high-order Nyström discretization," *J. Comput. Phys.*, vol. 146, no. 2, pp. 627–663, 1998.

[29] J. M. Song and W. C. Chew, "Moment method solutions using parametric geometry," *J. Electromagn. Waves Applicat.*, vol. 9, no. 1/2, pp. 71–83, Jan.-Feb. 1995.

[30] A. F. Peterson and K. R. Aberegg, "Parametric mapping of vector basis functions for surface integral equation formulations," *Appl. Computat. Electromagn. Soc. (ACES) J.*, vol. 10, pp. 107–115, Nov. 1995.

[31] K. R. Aberegg, A. Taguchi, and A. F. Peterson, "Application of higher-order vector basis functions to surface integral equation formulations," *Radio Sci.*, vol. 31, no. 5, pp. 1207–1213, Sep.-Oct. 1996.

[32] A. F. Peterson, "Accuracy of currents produced by the locally-corrected Nyström method and the method of moments when used with higher-order representations," *Appl. Computat. Electromagn. Soc. (ACES) J.*, vol. 17, no. 1, pp. 74–83, 2002.

[33] A. F. Peterson and M. M. Bibby, "Error trends in higher-order discretizations of the EFIE and MFIE," in *2005 IEEE APS Int. Symp. Dig.*, Washington, DC, Jul. 3–8, 2005, vol. 3A.

[34] M. I. Sancer, R. L. McClary, and K. J. Glover, "Electromagnetic computation using parametric geometry," *Electromagnetics*, vol. 10, pp. 85–103, 1990.

[35] M. S. Ingber and R. H. Ott, "An application of the boundary element method to the magnetic field integral equation," *IEEE Trans. Antennas Propag.*, vol. 39, no. 5, pp. 606–611, May 1991.

[36] N. Y. Zhu and F. M. Landstorfer, "Application of curved parametric triangular and quadrilateral edge elements in the moment method solution of the EFIE," *IEEE Microw. Guided Wave Lett.*, vol. 3, pp. 319–321, Sep. 1993.

[37] J. Wang and J. P. Webb, "Hierarchal vector boundary elements and p-adaption for 3-D electromagnetic scattering," *IEEE Trans. Antennas Propag.*, vol. 45, no. 12, pp. 1869–1879, Dec. 1997.

[38] B. M. Kolundzija and B. D. Popovic, "Entire-domain Galerkin method for analysis of metallic antennas and scatterers," *Proc. Inst. Elect. Eng.*, vol. 140, pt. H, pp. 1–10, 1993.

[39] B. M. Kolundžija, "Accurate solution of square scatterer as benchmark for validation of electromagnetic modeling of plate structures," *IEEE Trans. Antennas Propag.*, vol. 46, no. 7, pp. 1009–1014, Jul. 1998.

[40] B. M. Kolundžija, "Electromagnetic modeling of composite metallic and dielectric structures," *IEEE Trans. Microw. Theory Tech.*, vol. 47, no. 7, pp. 1021–1032, Jul. 1999.

[41] B. M. Notaros, B. D. Popovic, J. P. Weem, R. A. Brown, and Z. Popovic, "Efficient large-domain MoM solutions to electrically large practical EM problems," *IEEE Trans. Microw. Theory Tech.*, vol. 49, no. 1, pp. 151–159, Jan. 2001.

[42] M. Djordjevic and B. M. Notaros, "Higher-order hierarchical basis functions with improved orthogonality properties for moment-method modeling of metallic and dielectric microwave structures," *Microw. Opt. Technol. Lett.*, vol. 37, no. 2, pp. 83–88, Apr. 2003.

[43] M. Djordjevic and B. M. Notaros, "Double higher order method of moments for surface integral equation modeling of metallic and dielectric antennas and scatterers," *IEEE Trans. Antennas Propag.*, vol. 52, no. 8, pp. 2118–2129, Aug. 2004.

[44] M. Djordjevic and B. M. Notaros, "Higher order hybrid method of moments—physical optics modeling technique for radiation and scattering from large perfectly conducting surfaces," *IEEE Trans. Antennas Propag.*, vol. 53, no. 2, pp. 800–813, Feb. 2005.

[45] E. Jørgensen, J. L. Volakis, P. Meincke, and O. Breinbjerg, "Higher order hierarchical Legendre basis functions for electromagnetic modeling," *IEEE Trans. Antennas Propag.*, vol. 52, no. 11, pp. 2985–2995, Nov. 2004.

[46] E. Jørgensen, P. Meincke, and O. Breinbjerg, "A hybrid PO – Higher-order hierarchical MoM formulation using curvilinear geometry modeling," in *2003 IEEE Antennas Propag. Soc. Int. Symp. Dig.*, Columbus, OH, Jun. 22–27, 2003, vol. 4, pp. 98–101.

[47] K. C. Donepudi, J. Song, J. M. Jin, G. Kang, and W. C. Chew, "A novel implementation of multilevel fast multipole algorithm for higher order Galerkin's method," *IEEE Trans. Antennas Propag.*, vol. 48, no. 8, pp. 1192–1197, Aug. 2000.

[48] S. Y. Chen, W. C. Chew, J. M. Song, and J. S. Zhao, "Analysis of low frequency scattering from penetrable scatterers," *IEEE Trans. Geosci. Remote Sens.*, vol. 39, no. 4, pp. 726–735, Apr. 2001.

[49] G. Kang, J. Song, W. C. Chew, K. C. Donepudi, and J. M. Jin, "A novel grid-robust higher order vector basis function for the method of moments," *IEEE Trans. Antennas Propag.*, vol. 49, no. 6, pp. 908–915, Jun. 2001.

[50] K. C. Donepudi, J. M. Jin, S. Velamparambil, J. Song, and W. C. Chew, "A higher order parallelized multilevel fast multipole algorithm for 3-D scattering," *IEEE Trans. Antennas Propag.*, vol. 49, no. 7, pp. 1069–1078, Jul. 2001.

[51] F. Ling, J. Liu, and J. M. Jin, "Efficient electromagnetic modeling of three-dimensional multilayer microstrip antennas and circuits," *IEEE Trans. Microw. Theory Tech.*, vol. 50, no. 6, pp. 1682–1635, Jun. 2002.

[52] K. C. Donepudi, J. M. Jin, and W. C. Chew, "A higher order multilevel fast multipole algorithm for scattering from mixed conducting/dielectric bodies," *IEEE Trans. Antennas Propag.*, vol. 51, no. 10, pp. 2814–2821, Oct. 2003.

[53] R. A. Wildman, G. Pisharody, D. S. Weile, S. Balasubramaniam, and E. Michielssen, "An accurate scheme for the solution of the time-domain integral equations of electromagnetics using higher order vector bases and bandlimited extrapolation," *IEEE Trans. Antennas Propag.*, vol. 52, no. 11, pp. 2973–2984, Nov. 2004.

[54] R. A. Wildman and D. S. Weile, "An accurate broad-band method of moments using higher order basis functions and tree-loop decomposition," *IEEE Trans. Antennas Propag.*, vol. 52, no. 11, pp. 3005–3011, Nov. 2004.

[55] S. D. Gedney, "On deriving a locally corrected Nyström scheme from a quadrature sampled moment method," *IEEE Trans. Antennas Propag.*, vol. 51, no. 9, pp. 2402–2412, Sep. 2003.

[56] S. D. Gedney, A. Zhu, and C. C. Lu, "Study of mixed-order basis functions for the locally corrected Nyström method," *IEEE Trans. Antennas Propag.*, vol. 52, no. 11, pp. 2996–3004, Nov. 2004.

[57] A. Zhu, S. D. Gedney, and J. L. Visher, "A study of combined field formulations for material scattering for a locally corrected Nyström discretization," *IEEE Trans. Antennas Propag.*, vol. 53, no. 12, pp. 4111–4120, Dec. 2005.

[58] M. S. Tong and W. C. Chew, "A higher-order Nyström scheme for electromagnetic scattering by arbitrarily shaped surfaces," *IEEE Antennas Wireless Propag. Lett.*, vol. 4, pp. 277–280, 2005.

[59] W. Cai, T. Yu, H. Wang, and Y. Yu, "High-order mixed RWG basis functions for electromagnetic applications," *IEEE Trans. Microw. Theory Tech.*, vol. 49, no. 7, pp. 1295–1303, Jul. 2001.

[60] O. P. Bruno and A. Sei, "A fast high-order solver for EM scattering from complex penetrable bodies: TE case," *IEEE Trans. Antennas Propag.*, vol. 45, no. 12, pp. 1862–1864, Dec. 2000.

[61] O. P. Bruno and A. Sei, "A fast high-order solver for problems of scattering by heterogeneous bodies," *IEEE Trans. Antennas Propag.*, vol. 51, no. 11, pp. 3142–3154, Nov. 2003.

[62] W. J. Brown and D. R. Wilton, "Singular basis functions and curvilinear triangles in the solution of the electric field integral equation," *IEEE Trans. Antennas Propag.*, vol. 47, no. 2, pp. 347–353, Feb. 1999.

[63] B. D. Popović, M. D. Dragović, and A. R. Djordjević, *Analysis and Synthesis of Wire Antennas*. Chichester/New York: Research Studies Press/Wiley, 1982.

[64] B. D. Popović, *CAD of Wire Antennas and Related Radiating Structures*. Chichester/New York: Research Studies Press/Wiley, 1991.

[65] A. F. Peterson and M. M. Bibby, "High-order numerical solutions of the MFIE for the linear dipole," *IEEE Trans. Antennas Propag.*, vol. 52, no. 10, pp. 2684–2691, Oct. 2004.

[66] N. J. Champagne, D. R. Wilton, and J. D. Rockway, "The analysis of thin wires using higher order elements and basis functions," *IEEE Trans. Antennas Propag.*, vol. 54, no. 12, pp. 3815–3821, Dec. 2006.

[67] A. Mohan and D. S. Weile, "Convergence properties of higher order modeling of the cylindrical wire kernel," *IEEE Trans. Antennas Propag.*, vol. 55, no. 5, pp. 1318–1324, May 2007.

[68] R. D. Graglia, "The use of parametric elements in the moment method solution of static and dynamic volume integral equations," *IEEE Trans. Antennas Propag.*, vol. 36, no. 5, pp. 636–646, May 1988.

[69] B. D. Popovic and B. M. Notaros, "Entire-domain polynomial approximation of volume currents in the analysis of dielectric scatterers," *IEE Proc. – Microw., Antennas Propag.*, vol. 142, no. 3, pp. 207–212, Jun. 1995.

[70] B. M. Notaros and B. D. Popovic, "General entire-domain method for analysis of dielectric scatterers," *IEE Proc. – Microw., Antennas Propag.*, vol. 143, no. 6, pp. 498–504, Dec. 1996.

[71] B. M. Notaros and B. D. Popovic, "Optimized entire-domain moment-method analysis of 3D dielectric scatterers," *Int. J. Numerical Modelling: Electronic Networks, Devices and Fields*, vol. 10, pp. 177–192, 1997.

[72] B. M. Notaros and B. D. Popovic, "General entire-domain Galerkin method for analysis of wire antennas in the presence of dielectric bodies," *IEE Proc. – Microw., Antennas Propag.*, vol. 145, no. 1, pp. 13–18, Feb. 1998.

[73] P. De Doncker, "A potential integral equations method for electromagnetic scattering by penetrable bodies," *IEEE Trans. Antennas Propag.*, vol. 49, no. 7, pp. 1037–1042, Jul. 2001.

[74] K. Sertel and J. L. Volakis, "Method of moments solution of volume integral equations using parametric geometry modeling," *Radio Sci.*, vol. 37, no. 1, pp. 10–17, Jan.-Feb. 2002.

[75] O. S. Kim, E. Jørgensen, P. Meincke, and O. Breinbjerg, "Method of moments solution of volume integral equations using higher-order hierarchical Legendre basis functions," *Radio Sci.*, vol. 39, no. 5, pp. RS5003-1–RS5003-7, Sep. 2004.

[76] M. M. Botha, "Solving the volume integral equations of electromagnetic scattering," *J. Computat. Phys.*, vol. 218, pp. 141–158, 2006.

[77] M. M. Botha, "Fully hierarchical divergence-conforming basis functions on tetrahedral cells, with applications," *Int. J. Numer. Meth. Eng.*, vol. 71, pp. 127–148, 2007.

[78] B. M. Notaros and B. D. Popovic, "Large-domain integral-equation method for analysis of general 3-D electromagnetic structures," *IEE Proc. – Microw., Antennas Propag.*, vol. 145, no. 6, pp. 491–495, Dec. 1998.

[79] S. D. Gedney and C. C. Lu, "High-order integral equation solution for scattering by composite materials," in *2003 IEEE Antennas Propag. Soc. Int. Symp. Dig.*, Columbus, OH, Jun. 22–27, 2003, vol. 4, pp. 1055–1058.

[80] J. C. Nedelec, "Mixed finite elements in $\mathfrak{R}^3$," *Numerische Mathematik*, vol. 35, pp. 315–341, 1980.

[81] J. C. Nedelec, "A new family of mixed finite elements in $\mathfrak{R}^3$," *Numerische Mathematik*, vol. 50, pp. 57–81, 1986.

[82] R. Miniowitz and J. P. Webb, "Covariant-projection quadrilateral elements for the analysis of waveguides with sharp edges," *IEEE Trans. Microw. Theory Tech.*, vol. 39, no. 3, pp. 501–505, Mar. 1991.
[83] J. S. Wang and N. Ida, "Curvilinear and higher order "edge" finite elements in electromagnetic field computation," *IEEE Trans. Magn.*, vol. 29, no. 2, pp. 1491–1493, Mar. 1993.
[84] B. M. Dillon and J. P. Webb, "A comparison of formulations for the vector finite element analysis of waveguides," *IEEE Trans. Microw. Theory Tech.*, vol. 42, no. 2, pp. 308–316, Feb. 1994.
[85] G. E. Antilla and N. G. Alexopoulos, "Scattering from complex three-dimensional geometries by a curvilinear hybrid finite element-integral equation approach," *J. Opt. Soc. Amer. A*, vol. 11, no. 4, pp. 1445–1457, Apr. 1994.
[86] K. Hirayama, S. Alam, Y. Hayashi, and M. Koshiba, "Vector finite element method with mixed-interpolation-type triangular-prism element for waveguide discontinuities," *IEEE Trans. Microw. Theory Tech.*, vol. 42, no. 12, pp. 2311–2316, Dec. 1994.
[87] R. S. Preissig and A. F. Peterson, "A rationale for p-refinement with the vector Helmholtz equation and two-dimensional vector finite elements," *Appl. Computat. Electromagn. Soc. (ACES) J.*, vol. 19, no. 2, pp. 65–75, Jul. 2004.
[88] J. S. Savage and A. F. Peterson, "Higher-order vector finite elements for tetrahedral cells," *IEEE Trans. Microw. Theory Tech.*, vol. 44, no. 6, pp. 874–879, Jun. 1996.
[89] T. V. Yioultsis and T. D. Tsiboukis, "Development and implementation of second and third order vector finite elements in various 3-D electromagnetic field problems," *IEEE Trans. Magn.*, vol. 33, no. 2, pp. 1812–1815, Mar. 1997.
[90] X. Q. Sheng and S. Xu, "An efficient high-order mixed-edge rectangular-element method for lossy anisotropic dielectric waveguides," *IEEE Trans. Microw. Theory Tech.*, vol. 45, no. 7, pp. 1009–1013, Jul. 1997.
[91] J. P. Webb, "Hierarchical vector basis functions of arbitrary order for triangular and tetrahedral finite elements," *IEEE Trans. Antennas Propag.*, vol. 47, no. 8, pp. 1244–1253, Aug. 1999.
[92] Z. Huang and J. P. Webb, "Iterative solvers for hierarchical vector finite element analysis of microwave problems," *IEEE Trans. Magn.*, vol. 37, no. 5, pt. 1, pp. 3285–3288, Sep. 2001.
[93] J. Liu and J. M. Jin, "A novel hybridization of higher order finite element and boundary integral methods for electromagnetic scattering and radiation problems," *IEEE Trans. Antennas Propag.*, vol. 49, no. 12, pp. 1794–1806, Dec. 2001.
[94] J. Liu and J. M. Jin, "A special higher order finite-element method for scattering by deep cavities," *IEEE Trans. Antennas Propag.*, vol. 48, no. 5, pp. 694–703, May 2000.
[95] J. M. Jin, J. Liu, Z. Lou, and C. S. T. Liang, "A fully high-order finite-element simulation of scattering by deep cavities," *IEEE Trans. Antennas Propag.*, vol. 51, no. 9, pp. 2420–2429, Sep. 2003.
[96] E. A. Dunn, J. K. Byun, E. D. Branch, and J. M. Jin, "Numerical simulation of BOR scattering and radiation using a higher order FEM," *IEEE Trans. Antennas Propag.*, vol. 54, no. 3, pp. 945–952, Mar. 2006.
[97] D. Jiao, A. A. Ergin, B. Shanker, E. Michielssen, and J. M. Jin, "A fast higher-order time-domain finite element-boundary integral method for 3-D electromagnetic scattering analysis," *IEEE Trans. Antennas Propag.*, vol. 50, no. 9, pp. 1192–1202, Sep. 2002.
[98] R. D. Graglia, D. R. Wilton, A. F. Peterson, and I. L. Gheorma, "Higher order interpolatory vector bases on prism elements," *IEEE Trans. Antennas Propag.*, vol. 46, no. 3, pp. 442–450, Mar. 1998.
[99] R. D. Graglia and I. L. Gheorma, "Higher order interpolatory vector bases on pyramidal elements," *IEEE Trans. Antennas Propag.*, vol. 47, no. 5, pp. 775–782, May 1999.
[100] P. Savi, I. L. Gheorma, and R. D. Graglia, "Full-wave high-order FEM model for lossy anisotropic waveguides," *IEEE Trans. Microw. Theory Tech.*, vol. 50, no. 2, pp. 495–500, Feb. 2002.
[101] R. D. Graglia and G. Lombardi, "Singular higher order complete vector bases for finite methods," *IEEE Trans. Antennas Propag.*, vol. 52, no. 7, pp. 1672–1685, Jul. 2004.
[102] M. M. Ilic and B. M. Notaros, "Higher order hierarchical curved hexahedral vector finite elements for electromagnetic modeling," *IEEE Trans. Microw. Theory Tech.*, vol. 51, no. 3, pp. 1026–1033, Mar. 2003.
[103] M. M. Ilic and B. M. Notaros, "Higher order large-domain hierarchical FEM technique for electromagnetic modeling using Legendre basis functions on generalized hexahedra," *Electromagnetics*, vol. 26, no. 7, pp. 517–529, Oct. 2006.
[104] M. M. Ilic, A. Z. Ilic, and B. M. Notaros, "Higher order large-domain FEM modeling of 3-D multiport waveguide structures with arbitrary discontinuities," *IEEE Trans. Microw. Theory Tech.*, vol. 52, no. 6, pp. 1608–1614, Jun. 2004.
[105] M. M. Ilic, A. Z. Ilic, and B. M. Notaros, "Efficient large-domain 2-D FEM solution of arbitrary waveguides using p-refinement on generalized quadrilaterals," *IEEE Trans. Microw. Theory Tech.*, vol. 53, no. 4, pp. 1377–1383, Apr. 2005.
[106] J. H. Lee, T. Xiao, and Q. H. Liu, "A 3-D spectral-element method using mixed-order curl conforming vector basis functions for electromagnetic fields," *IEEE Trans. Microw. Theory Tech.*, vol. 54, no. 1, pp. 437–444, Jan. 2006.
[107] L. S. Andersen and J. L. Volakis, "Development and application of a novel class of hierarchical tangential vector finite elements for electromagnetics," *IEEE Trans. Antennas Propag.*, vol. 47, no. 1, pp. 112–120, Jan. 1999.
[108] L. S. Andersen and J. L. Volakis, "Accurate and efficient simulation of antennas using hierarchical mixed-order tangential vector finite elements for tetrahedra," *IEEE Trans. Antennas Propag.*, vol. 47, no. 8, pp. 1240–1243, Aug. 1999.
[109] L. S. Andersen and J. L. Volakis, "Condition numbers for various FEM matrices," *J. Electromagn. Waves Applicat.*, vol. 13, pp. 1663–1679, 1999.
[110] J. S. Juntunen and T. D. Tsiboukis, "On the FEM treatment of wedge singularities in waveguide problems," *IEEE Trans. Microw. Theory Tech.*, vol. 48, no. 6, pp. 1030–1037, Jun. 2000.
[111] E. Martini, G. Pelosi, and S. Selleri, "A hybrid finite-element–modal-expansion method with a new type of curvilinear mapping for the analysis of microwave passive devices," *IEEE Trans. Microw. Theory Tech.*, vol. 51, no. 6, pp. 1712–1717, Jun. 2003.
[112] D. K. Sun and Z. Cendes, "Fast high-order FEM solutions of dielectric wave guiding structures," *IEE Proc. – Microw., Antennas Propag.*, vol. 150, no. 4, pp. 230–236, Aug. 2003.
[113] S. C. Lee, J. F. Lee, and R. Lee, "Hierarchical vector finite elements for analyzing waveguiding structures," *IEEE Trans. Microw. Theory Tech.*, vol. 51, no. 8, pp. 1897–1905, Aug. 2003.
[114] D. K. Sun, J. F. Lee, and Z. Cendes, "The transfinite-element time-domain method," *IEEE Trans. Microw. Theory Tech.*, vol. 51, no. 10, pp. 2097–2105, Oct. 2003.
[115] J. F. Lee and D. K. Sun, "p-type multiplicative Schwarz (pMUS) method with vector finite elements for modeling three-dimensional waveguide discontinuities," *IEEE Trans. Microw. Theory Tech.*, vol. 52, no. 3, pp. 864–870, Mar. 2004.
[116] R. N. Rieben, D. A. White, and G. H. Rodrigue, "Improved conditioning of finite element matrices using new high-order interpolatory bases," *IEEE Trans. Antennas Propag.*, vol. 52, no. 10, pp. 2675–2683, Oct. 2004.
[117] M. M. Botha and J. M. Jin, "Adaptive finite element-boundary integral analysis for electromagnetic fields in 3-D," *IEEE Trans. Antennas Propag.*, vol. 53, no. 5, pp. 1710–1720, May 2005.
[118] N. Marais and D. B. Davidson, "Numerical evaluation of hierarchical vector finite elements on curvilinear domains in 2-D," *IEEE Trans. Antennas Propag.*, vol. 54, no. 2, pp. 734–738, Feb. 2006.
[119] F. G. Hu, C. F. Wang, and Y. B. Gan, "Efficient calculation of interior scattering from large three-dimensional PEC cavities," *IEEE Trans. Antennas Propag.*, vol. 55, no. 1, pp. 167–177, Jan. 2007.
[120] M. Fusco, "FDTD algorithm in curvilinear coordinates," *IEEE Trans. Antennas Propag.*, vol. 38, no. 1, pp. 76–88, Jan. 1990.
[121] J. F. Lee, R. Pandalech, and R. Mittra, "Modeling three-dimensional discontinuities in waveguides using nonorthogonal FDTD algorithm," *IEEE Trans. Microw. Theory Tech.*, vol. 40, no. 2, pp. 346–352, Feb. 1992.
[122] M. F. Hadi and M. Piket-May, "A modified FDTD (2, 4) scheme for modeling electrically large structures with high-phase accuracy," *IEEE Trans. Antennas Propag.*, vol. 45, no. 2, pp. 254–264, Feb. 1997.
[123] E. Turkel, "High-order methods," in *Advances in Computational Electrodynamics: The Finite-Difference Time-Domain Method*, A. Taflove, Ed. Norwood, MA: Artech House, 1998, ch. 2, pp. 63–110.
[124] N. V. Kantartzis and T. D. Tsiboukis, "A higher-order FDTD technique for the implementation of enhanced dispersionless perfectly matched layers combined with efficient absorbing boundary conditions," *IEEE Trans. Magn.*, vol. 34, no. 5, pt. 1, pp. 2736–2739, Sep. 1998.
[125] A. Yefet and P. G. Petropoulos, "A staggered fourth-order accurate explicit finite difference scheme for the time-domain Maxwell's equations," *J. Comput. Phys.*, vol. 168, pp. 286–315, 2001.
[126] S. V. Georgakopoulos, C. R. Birtcher, C. A. Balanis, and R. A. Renaut, "Higher-order finite-difference schemes for electromagnetic radiation, scattering, and penetration: Part I—Theory," *IEEE Antennas Propag. Mag.*, vol. 44, no. 2, pp. 134–142, Feb. 2002.
[127] Y. S. Chung, T. K. Sarkar, B. H. Jung, and M. S. Palma, "An unconditionally stable scheme for the finite-difference time-domain method," *IEEE Trans. Microw. Theory Tech.*, vol. 51, no. 3, pp. 697–704, Mar. 2003.

[128] Z. Shao, Z. Shen, Q. He, and G. Wei, "A generalized higher order finite-difference time-domain method and its application to guided-wave problems," *IEEE Trans. Microw. Theory Tech.*, vol. 51, no. 3, pp. 856–861, Mar. 2003.
[129] N. V. Kantartzis and T. D. Tsiboukis, "A higher order nonstandard FDTD-PML method for the advanced modeling of complex EMC problems in generalized 3-D curvilinear coordinates," *IEEE Trans. Electromagn. Compatibil.*, vol. 46, no. 2, pp. 2–11, Feb. 2004.
[130] T. T. Zygiridis and T. D. Tsiboukis, "Development of higher order FDTD schemes with controllable dispersion error," *IEEE Trans. Antennas Propag.*, vol. 53, no. 9, pp. 2952–2960, Sep. 2005.
[131] H. Spachmann, R. Schuhmann, and T. Weiland, "Higher order explicit time integration schemes for Maxwell's equations," *Int. J. Numer. Modelling: Electron. Networks, Devices and Fields*, vol. 15, pp. 419–437, 2002.
[132] K. A. Michalski and J. R. Mosig, "Multilayered media Green's functions in integral equation formulations," *IEEE Trans. Antennas Propag.*, vol. 45, no. 3, pp. 508–519, Mar. 1997.
[133] R. Bartels, J. Beatty, and B. Barsky, *An Introduction to Splines for use in Computer Graphics and Geometric Modeling*. New York: Elsevier, 1995.
[134] R. York, R. C. Compton, and B. J. Rubin, "Experimental verification of the 2-D rooftop approach for modeling microstrip patch antennas," *IEEE Trans. Antennas Propag.*, vol. 39, no. 5, pp. 690–694, May 1991.
[135] *Handbook of Mathematical Functions With Formulas, Graphs and Mathematical Tables*, M. Abramowitz and I. A. Stegun, Eds. New York: Dover, 1972, ch. 22, pp. 771–802.
[136] S. M. Rao, D. R. Wilton, and A. W. Glisson, "Electromagnetic scattering by surfaces of arbitrary shape," *IEEE Trans. Antennas Propag.*, vol. 30, no. 5, pp. 409–418, May 1982.
[137] E. J. Nyström, "Über die Praktische Auflösung von Integralgleichungen mit Anwendungen auf Randwertaufgaben," *Acta Mathematica.*, vol. 54, no. 1, pp. 185–204, Jul. 1930.
[138] J. Van Bladel, *Electromagnetic Fields*. New York: McGraw-Hill, 1964.
[139] M. M. Bibby and A. F. Peterson, "High accuracy calculation of the magnetic vector potential on surfaces," *Appl. Computat. Electromagn. Soc. (ACES) J.*, vol. 18, no. 1, pp. 12–22b, Mar. 2003.
[140] M. M. Bibby and A. F. Peterson, "High accuracy evaluation of the EFIE matrix entries on a planar patch," *Appl. Computat. Electromagn. Soc. (ACES) J.*, vol. 20, no. 3, pp. 198–206, Nov. 2005.
[141] S. Järvenpää, M. Taskinen, and P. Ylä-Oijala, "Singularity subtraction technique for high-order polynomial vector basis functions on planar triangles," *IEEE Trans. Antennas Propag.*, vol. 54, no. 1, pp. 42–49, Jan. 2006.
[142] M. G. Duffy, "Quadrature over a pyramid or cube of integrands with a singularity at a vertex," *SIAM J. Numer. Anal.*, vol. 19, no. 6, pp. 1260–1262, 1982.
[143] D. J. Taylor, "Accurate and efficient numerical integration of weakly singular integrals in Galerkin EFIE solutions," *IEEE Trans. Antennas Propag.*, vol. 51, no. 7, pp. 1630–1637, Jul. 2003.
[144] M. A. Khayat and D. R. Wilton, "Numerical evaluation of singular and near-singular potential integrals," *IEEE Trans. Antennas Propag.*, vol. 53, no. 10, pp. 3180–3190, Oct. 2005.
[145] B. Shanker, A. A. Ergin, M. Lu, and E. Michielssen, "Fast analysis of transient electromagnetic scattering phenomena using the multilevel plane wave time domain algorithm," *IEEE Trans. Antennas Propag.*, vol. 51, no. 3, pp. 628–641, Mar. 2003.
[146] A. Greenbaum, *Iterative Methods for Solving Linear Systems*. Philadelphia, PA: SIAM, 1997.
[147] H. A. van Der Vorst, "BI-CGSTAB: A fast and smoothly converging variant of BI-CG for the solution of nonsymmetric linear systems," *SIAM J. Sci. Statist. Comput.*, vol. 13, pp. 631–644, 1992.
[148] P. Sonneveld, "CGS: A fast Lanczos-type solver for nonsymmetric linear systems," *SIAM J. Sci. Statist. Comput.*, vol. 10, pp. 36–52, 1989.
[149] Y. Saad, "GMRES: A generalized minimal residual algorithm for solving nonsymmetric linear systems," *SIAM J. Sci. Statist. Comput.*, vol. 7, pp. 856–869, 1986.
[150] R. W. Freund, "A transpose-free quasi-minimal residual algorithm for non-Hermitian linear systems," *SIAM J. Sci. Comput.*, vol. 14, no. 2, pp. 470–482, 1993.
[151] J. W. H. Liu, "The multifrontal method for sparse matrix solution: Theory and practice," *SIAM Rev.*, vol. 34, pp. 82–109, 1992.
[152] M. Benzi, "Preconditioning techniques for large linear systems: A survey," *J. Computat. Phys.*, vol. 182, pp. 418–477, 2002.
[153] A. F. Peterson, D. R. Wilton, and R. E. Jorgenson, "Variational nature of Galerkin and non-Galerkin moment method solutions," *IEEE Trans. Antennas Propag.*, vol. 44, no. 4, pp. 500–503, Apr. 1996.
[154] K. F. Warnick and W. C. Chew, "Accuracy of the method of moments for scattering by a cylinder," *IEEE Trans. Microw. Theory Tech.*, vol. 48, no. 10, pp. 1652–1660, Oct. 2000.
[155] K. F. Warnick and W. C. Chew, "Error analysis of surface integral equation methods," in *Fast and Efficient Algorithms in Computational Electromagnetics*, W. C. Chew, J.-M. Jin, E. Michielssen, and J. Song, Eds. Norwood, MA: Artech House, 2001.
[156] K. F. Warnick and W. C. Chew, "Error analysis of the moment method," *IEEE Antennas Propag. Mag.*, vol. 46, no. 6, pp. 38–53, Dec. 2004.
[157] C. P. Davis and K. F. Warnick, "High-order convergence with a low-order discretization of the 2-D MFIE," *IEEE Antennas Wireless Propag. Lett.*, vol. 3, pp. 355–358, 2004.
[158] C. P. Davis and K. F. Warnick, "Error analysis of 2-D MoM for MFIE/EFIE/CFIE based on the circular cylinder," *IEEE Trans. Antennas Propag.*, vol. 53, no. 1, pp. 321–331, Jan. 2005.
[159] C. P. Davis and K. F. Warnick, "On the physical interpretation of the Sobolev norm in error estimation," *Appl. Computat. Electromagn. Soc. (ACES) J.*, vol. 20, no. 2, pp. 144–150, Jul. 2005.
[160] E. F. Kuester, "Computable error bounds for variational functionals of solutions of a convolution integral equations of the first kind," *Wave Motion*, vol. 22, pp. 171–185, 1995.
[161] F. J. C. Meyer and D. B. Davidson, "A posteriori error estimates for two-dimensional electromagnetic field computations: Boundary elements and finite elements," *Appl. Computat. Electromagn. Soc. (ACES) J.*, vol. 11, no. 2, pp. 40–54, 1996.
[162] B. M. Kolundzija and V. V. Petrovic, "Power conservation in method of moments and finite-element method for radiation problems," *IEEE Trans. Antennas Propag.*, vol. 53, no. 8, pp. 2728–2737, Aug. 2005.
[163] X. Luo, M. S. Shephard, R. M. O'Bara, R. Nastasia, and M. W. Beall, "Automatic p-version mesh generation for curved domains," *Engineering With Computers*, vol. 20, no. 3, pp. 265–285, Sep. 2004.
[164] S. J. Sherwin and J. Peiró, "Mesh generation in curvilinear domains using high-order elements," *Int. J. Numer. Meth. Eng.*, vol. 53, no. 1, pp. 207–223, Jan. 2002.
[165] M. Tasić and B. Kolundžija, "Efficient electromagnetic modeling based on automated quadrilateral meshing of polygons," *Engineering Analysis With Boundary Elements*, vol. 27, no. 4, pp. 361–373, Apr. 2003.
[166] A. Ž Ilić, M. M. Ilić, and B. M. Notaroš, "On the higher-order hexahedral meshing for FEM in electromagnetics," in *2004 IEEE AP-S Int. Symp. Antennas and Propagation and USNC/URSI National Radio Science Meeting, URSI Dig.*, Monterey, CA, Jun. 20–26, 2004.
[167] A. H. Stroud, *Approximate Calculation of Multiple Integrals*. Englewood Cliffs, NJ: Prentice-Hall, 1971.
[168] A. Chatterjee, J. M. Jin, and J. L. Volakis, "Computation of cavity resonances using edge-based finite elements," *IEEE Trans. Microw. Theory Tech.*, vol. 40, no. 11, pp. 2106–2108, Nov. 1992.
[169] J. S. Wang and N. Ida, "Eigenvalue analysis in electromagnetic cavities using divergence free finite elements," *IEEE Trans. Magn.*, vol. 27, no. 5, pp. 3978–3981, Sep. 1991.
[170] A. Nakatani and N. G. Alexopoulos, "Coupled microstrip lines on a cylindrical substrate," *IEEE Trans. Microw. Theory Tech.*, vol. 35, no. 12, pp. 1392–1398, Dec. 1987.

Branislav M. Notaroš (M'00–SM'03) was born in Zrenjanin, Yugoslavia, in 1965. He received the Dipl.Ing. (B.Sc.), M.Sc., and Ph.D. degrees in electrical engineering from the University of Belgrade, Belgrade, Yugoslavia, in 1988, 1992, and 1995, respectively.

From 1996 to 1998, he was an Assistant Professor in the Department of Electrical Engineering at the University of Belgrade. He spent the 1998–1999 academic year as a Research Associate at the University of Colorado at Boulder. He was an Assistant Professor from 1999 to 2004 and an Associate Professor, from 2004 to 2006 in the Department of Electrical and Computer Engineering at the University of Massachusetts, Dartmouth. He is currently an Associate Professor of electrical and computer engineering at Colorado State University, Fort Collins. His research and teaching interests and activities are in theoretical and computational electromagnetics and in antennas and microwaves. His publications include about 70 journal and conference papers, and five textbooks and workbooks.

Dr. Notaroš was the recipient of the 2005 IEEE MTT-S Microwave Prize, 1999 IEE Marconi Premium, and 2005 UMass Dartmouth Scholar of the Year Award.